*Journal of Microscopy, Vol. 232, Pt 3 2008, pp. 562–579*
*Received 4 July 2007; accepted 2 March 2008*

# Comparison of single-particle analysis and electron tomography approaches: an overview

S. JONIĆ*, C.O.S. SORZANO† & N. BOISSET*
**Université Pierre et Marie Curie, IMPMC-UMR7590, Paris, F-75005 France; and CNRS, IMPMC-UMR7590, Paris, F-75005 France*
*†Bioengineering Lab. Escuela Politécnica Superior. Univ. San Pablo CEU. Campus Urb. Montepríncipe s/n. 28668 Boadilla del Monte, Madrid, Spain*

**Key words.** Electron tomography, review, single-particle analysis, three-dimensional reconstruction, transmission electron microscopy.

**Summary**

Three-dimensional structure of a wide range of biological specimens can be computed from images collected by transmission electron microscopy. This information integrated with structural data obtained with other techniques (e.g., X-ray crystallography) helps structural biologists to understand the function of macromolecular complexes and organelles within cells. In this paper, we compare two three-dimensional transmission electron microscopy techniques that are becoming more and more related (at the image acquisition level as well as the image processing one): *electron tomography* and *single-particle analysis*. The first one is currently used to elucidate the three-dimensional structure of cellular components or smaller entire cells, whereas the second one has been traditionally applied to structural studies of macromolecules and macromolecular complexes. Also, we discuss possibilities for their integration with other structural biology techniques for an integrative study of living matter from proteins to whole cells.

## Introduction

Three-dimensional (3D) structural studies of biological matter, from proteins to whole cells, are of a great importance for fully understanding the function of macromolecular complexes and organelles within cells. The 3D structure of a cellular component is tightly related to its function within a cell, and the knowledge of both structure and function is necessary, for instance, to design drugs whose targets are particular proteins.

Correspondence to: S. Jonić. Tel: +33144277205; fax: +33144273785; e-mail: Slavica.Jonic@impmc.jussieu.fr

We are deeply saddened that we must report the loss of our friend and colleague Dr. Nicolas Boisset who passed away on January 4, 2008.

The quality of the 3D structure is usually expressed in terms of *resolution*, which measures the level of detail contained in the structure. High resolution means the possibility of interpreting the structure at a high level of detail, which is mandatory for understanding its function.

Several complementary techniques have been developed for determining the 3D structure of biological specimens. In the case of molecules that can either auto-assemble or be coerced to assemble in 3D crystals, X-ray diffraction is traditionally used to determine their atomic structure. Moreover, since the development of synchrotron radiation in the sixties, structural biology blossomed, and nowadays, several hundreds of macromolecular structures are solved each year by X-ray crystallography. However, a large number of macromolecules diffract poorly or cannot be crystallized. For such samples, alternative approaches must be used. For example, for particles with low molecular weight (lower than 30 kDa), nuclear magnetic resonance is a very powerful technique. For larger macromolecular assemblies (molecular weights higher than 30 kDa) and other, larger cellular components, 3D transmission electron microscopy (TEM) techniques are the best exploration methods.

Each 3D TEM technique requires a particular image acquisition protocol and a computational method for reconstruction of the 3D structure from the acquired images. Highest-resolution structures currently are those obtained from two-dimensional (2D) crystals and highly symmetrical particles because the signal-to-noise ratio (SNR) improves when averaging repeated objects or using the symmetry properties of the object. *Electron crystallography* is a TEM technique that can achieve atomic resolution, but it requires specimens that arrange in one-molecule-thick 2D crystalline arrays forming an ordered repetition of identical objects on a 2D real-space lattice (e.g., membrane proteins) (Walz & Grigorieff, 1998; Glaeser, 1999; Ellis & Hebert, 2001;

Hite *et al.*, 2007; Schmidt-Krey, 2007). The structure of highly symmetrical specimens such as helical structures (e.g., filamentous viruses, cytoskeletal and muscle filaments) or icosahedral structures (e.g., protein capsid of some viruses) can be solved at high resolution thanks to 3D TEM methods that do not require 2D crystals but rely on symmetry properties of the particle (*helical reconstruction methods* (DeRosier & Moore, 1970; Morgan & Rosier, 1992; Carragher *et al.*, 1996; Wang & Nogales, 2005; Egelman, 2007) and *icosahedral reconstruction methods* (Baker *et al.*, 1999; Conway & Steven, 1999; Thuman-Commike & Chiu, 2000; Navaza, 2003). Icosahedral reconstruction is often considered as a particular case of *single-particle analysis*, which is a more general method since it is not limited to symmetric particles. Actually, this is the only 3D TEM method that can be used currently to obtain a high-resolution reconstruction of non-crystalline and asymmetric particles under low-dose conditions (Tao & Zhang, 2000; van Heel *et al.*, 2000; Frank, 2002; Frank, 2006a; Ruiz & Radermacher, 2006; Wang & Sigworth, 2006). It relies on a combined use of images from a large number of structurally identical particles, and it is limited to particles with a size between 10 and 200 nm. Using single-particle analysis, the 3D structure of different specimens (i.e., structures with high symmetry, lower-symmetry structures and completely asymmetric structures) has been solved at resolutions between 15 and 6 Å (Gabashvili *et al.*, 2000; Ludtke *et al.*, 2004; Falke *et al.*, 2005; Fotin *et al.*, 2006; Saban *et al.*, 2006; Martin *et al.*, 2007). The only technique that allows currently obtaining the structure of large sub-cellular components (of size between 100 and 500 nm) and localizing macromolecular complexes in the context of the cell is *electron tomography* (Koster & Klumperman, 2003; Sali *et al.*, 2003; Subramaniam & Milne, 2004; Lucic *et al.*, 2005; McIntosh *et al.*, 2005; Frank, 2006b). This technique also has the ability of revealing the heterogeneous aspects of complex assemblies. However, no consistent estimation of the resolution has been established. In this context, several attempts have been made to estimate the size of reliable features seen in the reconstructed volumes (Cardone *et al.*, 2005). The estimated resolution lies somewhere between 10 and 4 nm (Nicastro *et al.*, 2000; O'Toole *et al.*, 2002; Grunewald *et al.*, 2003; Cyrklaff *et al.*, 2005; Marsh, 2005; Briggs *et al.*, 2006; Comolli *et al.*, 2006; Donohoe *et al.*, 2006; Bouchet-Marquis *et al.*, 2007).

Although electron crystallography and helical–icosahedral reconstruction techniques are limited to the study of specimens having some special properties (crystalline or highly symmetric, respectively), single-particle analysis (SPA) and electron tomography (ET) are more general techniques, whose potential for combining and correlating starts attracting attention of many structural biology labs that have been specialized for one of the techniques and are now adopting the other as well. The goal of this paper is to briefly describe and compare these two techniques in the light of their potential combination.

## Image acquisition

In this section, we present the main principles of SPA and ET reconstructions, techniques for specimen protection against radiation damages and possibilities for automated image acquisition.

### *Diffraction, Fourier transform, central slice theorem and common lines*

The Fourier transform plays a central role in image acquisition and in image processing for 3D reconstruction. In TEM, either an electron diffraction pattern in the back-focal plane or an image in the image plane can be recorded from an object. The space where the diffraction pattern forms is reciprocal space, whereas the space at the image plane is real space. The transformation from the real space to the reciprocal space is given by the Fourier transform. A diffraction pattern resembles the power spectrum (calculated from the Fourier transform) of the object that forms this diffraction pattern.

To explain the principle of 3D reconstruction, one usually uses the *central slice theorem* (DeRosier & Klug, 1968; Kak & Slaney, 1988). Thanks to this theorem, the 2D Fourier transforms of 2D projection images can be assembled in the 3D Fourier space, which then only should be inverted to provide the 3D real-space information about the structure of the studied specimen. More precisely, this theorem says that a central slice (i.e., a central plane) through the origin in reciprocal space corresponds to the projection in real space in a direction normal to the plane. Since any two central slices have a line in common (*common line*), a consequence of this theorem is that it is possible to determine the orientation of one projection plane with respect to other projection planes by determining a relative orientation of their common lines.

### *Principles of SPA and ET reconstructions*

SPA is used for studies of macromolecules and macromolecular assemblies whose structure and dynamic interactions can be analyzed *in vitro*, in isolation (e.g., proteins, ribosomes, viruses). The data collection for this approach consists in taking 2D projections of a sample containing many identical but differently oriented copies of the same object (Fig. 1(A)). Thus, when an even distribution of single particle orientations is observed on the specimen grid, this technique allows collecting all necessary data for the computation of a 3D average structure of the studied particles.

Conversely, ET is aimed at the study of systems maintaining their *in vivo* structural integrity as much as possible such as cells, cell portions or tissues, although it is also used for structural studies of isolated macromolecular complexes and organelles such as mitochondria (Nicastro *et al.*, 2000). The data for ET reconstruction are collected by

 

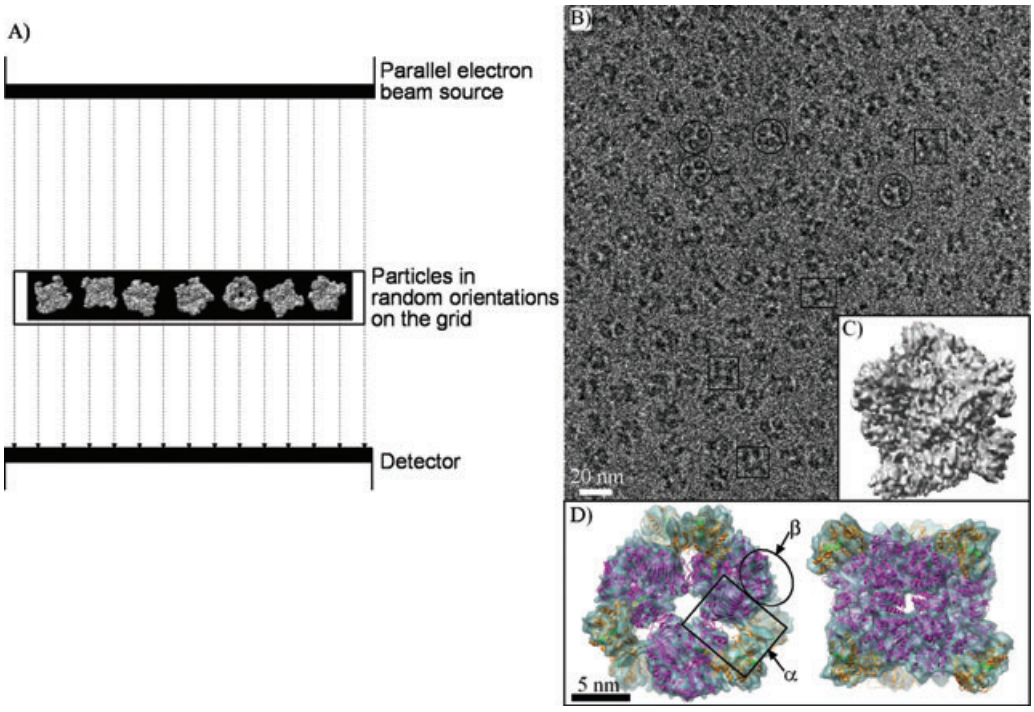


**Fig. 1.** Principle of single-particle analysis and an example. (A) Data collection geometry. The electron source, the detector and the specimen holder are stationary, whereas many identical copies of the same macromolecule are in different random orientations. An ideal 2D projection image is a parallel-beam projection of the sample's electrostatic potential (parallel dashed lines represent the electron beam). (B–D) Use of single-particle analysis to determine the 3D structural architecture of the multi-enzymatic complex *Glutamate synthase* (GltS) from *E. coli* [the figure was produced with the data used in Sorzano *et al.* (2007a); the GltS function was interpreted in Cottevieille *et al.* (2008) based on these data]. (B) 2D cryo-EM projection image of the GltS sample on a holey carbon film vitrified by plunge freezing in liquid ethane. The circles show the top views of the GltS, whereas the side views are shown using rectangles. The intermediate views, also visible in the image, are not highlighted. (C) Isosurface representation [Chimera (Goddard *et al.*, 2007)] of the reconstructed 3D structure at 9.5 Å resolution with $D_3$ point-group symmetry. (D) Fitting of atomic coordinates of $\alpha$ and $\beta$ sub-units [the GltS complex has the stoichiometry $(\alpha\beta)_6$] in the GltS reconstruction shown in (C). Top (left) and side (right) views of the structure shown in (C) with fitted atomic structures.

taking multiple 2D projections of the same specimen being gradually rotated around an axis perpendicular to the electron beam (Fig. 2(A)) or around two or more tilt axes (Penczek *et al.*, 1995; Mastronarde, 1997; Messaoudi *et al.*, 2006).

### *Structure preservation and contrast-enhancing methods*

Before image acquisition, biological specimens must be protected against radiation generated in or by the microscope; otherwise, the interaction of electrons with non-protected organic matter damages its structure (Glaeser, 1971). Radiation damage is reduced at low temperatures. Cryo-electron microscopy (cryo-EM) is a protection method that preserves the specimen structure in near-physiological conditions. This technique consists of embedding the specimen in vitreous water using a rapid-freezing method such as plunge-freezing, where the specimen is rapidly plunged into liquid ethane (c. –150°C) thereby dropping its temperature at an approximate rate of $10^4$°Cs$^{-1}$, followed by imaging of the frozen-hydrated specimens maintained at either liquid nitrogen or liquid helium temperatures (less than –160°C) (Dubochet *et al.*, 1988).

In the case of SPA, cryo-EM grids with specimens embedded in 60- to 100-nm-thick vitreous water are readily prepared from aqueous suspensions. However, a problem of cryo-EM is that the electron doses required for a good SNR lead to unacceptable specimen damage (Hayward & Glaeser, 1979). Therefore, to acquire high-resolution images, the electron dose must be kept at a low level [e.g., 10 electronsÅ$^{-2}$ in the case of SPA and a 200-kV microscope (Jonic *et al.*, 2007)]. This means that high-resolution images have a poor contrast and are dominated by noise (for an example of this type of image, see Fig. 1(B)).

Cryo-ET (ET of frozen-hydrated specimens) encounters at least three additional problems. First, the image contrast is low because of the small difference in mass density between unstained clusters of macromolecules and the frozen cytosol that surrounds them. It is therefore hard to visualize fine details of cellular sub-structure even when under-focussing

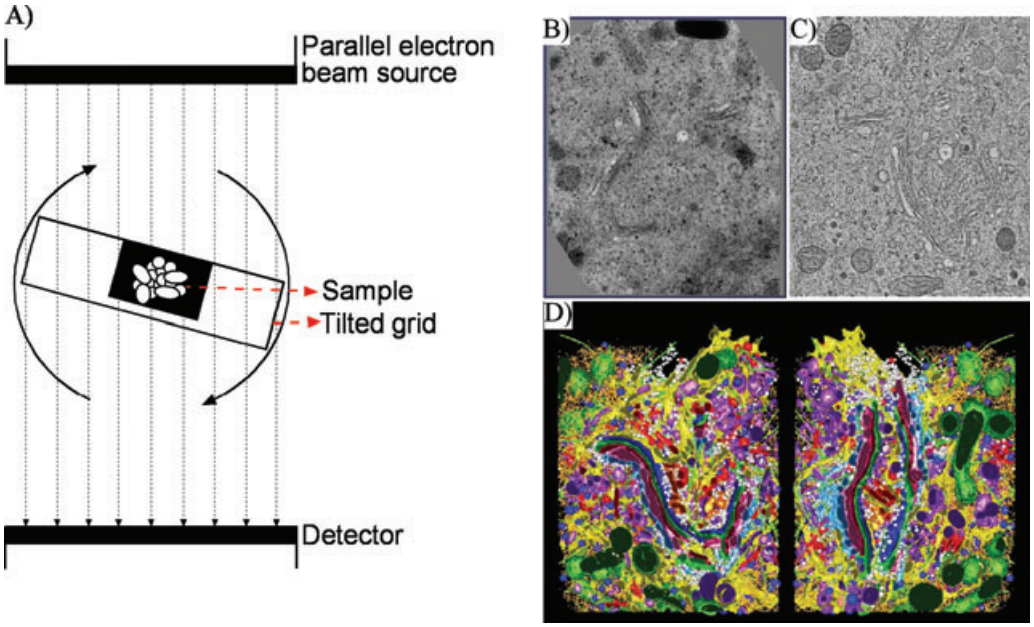


**Fig. 2.** Principle of electron tomography and an example. (A) Single-axis tilt geometry for data collection. The electron source and the detector are stationary, whereas the specimen holder is tilted by constant angular increments around an axis perpendicular to the electron beam (parallel dashed lines). (B–D) Use of electron tomography in determining the organization of the mammalian Golgi from the pancreatic beta cell line, HIT-T15 [reproduced from Marsh (2005), with permission from Elsevier]. (B) 2D projection image of a thick (400-nm) plastic section cut from an immortalized HIT-T15 prepared by high-pressure freezing and freeze substitution followed by plastic embedding. (C) Slice extracted from the volume computed using images from (B) and dual-axis tilt reconstruction at approximately 6 nm resolution. (D) Two views of the modelled (segmented) serially reconstructed Golgi region rotated by 180°, in the context of all surrounding organelles, vesicles, ribosomes and microtubules. Golgi cisternae (C1– C7); C1, light blue; C2, pink; C3, cherry red; C4, green; C5, dark blue; C6, gold; C7, bright red; endoplasmic reticulum, yellow; membrane-bound ribosomes, blue; free ribosomes, orange; microtubules, bright green; dense core vesicles, bright blue; clathrin-negative vesicles, white; clathrin-positive compartments and vesicles, bright red; clathrin-negative compartments and vesicles, purple; and mitochondria, dark green.

the microscope objective lens to produce phase contrast (McIntosh *et al.*, 2005).

Second, the method of plunge freezing gives the best results on relatively thin specimens (up to 500-nm-thick specimens, which include isolated organelles, small cells and thin parts of larger cells). Thicker specimens (e.g., thick parts of larger cells and tissues) are difficult to vitrify owing to lower cooling rates at the centre of the thick specimen (Studer *et al.*, 1989). To vitrify thicker samples while avoiding the formation of ice crystals and their damage to specimen, special instrumentation is required. With high-pressure freezing, samples as thick as 500 $\mu$m can be vitrified with no ice crystals (Studer *et al.*, 1989). Potential damaging effects of high pressure on the specimen structure are minimized if the pressure is increased quickly and followed immediately by rapid freezing.

The third problem encountered when using cryogenic techniques for ET is also related to the specimen thickness. Thick specimens should be cut in sections appropriate for electron microscopy (20–500 nm thick), whereas slices as thin as 20–100 nm may be required for a high-resolution serial section reconstruction (single images of individual thin sections are computationally merged to obtain a 3D reconstruction). Cutting of frozen-hydrated thick specimens at cryogenic temperatures is extremely difficult and many artefacts (such as knife marks, crevasses and compression) are generated during cryo-sectioning, which complicate the interpretation of the 3D reconstruction (Richter, 1994; Sartori Blanc *et al.*, 1998). The production of *cryo-sections* is an art currently practiced by relatively few laboratories (Al-Amoudi *et al.*, 2004a).

One alternative is to create plastic sections by freeze substitution; material is vitrified by high-pressure freezing and water is then substituted with organic solvents containing chemical fixatives at temperatures around –80°C (Zalokar, 1966; Kellenberger, 1991). The samples are warmed at a temperature around –40°C, embedded in plastic or resin and sectioned at room temperature. The contrast is often increased by post-staining with a heavy metal salt solution. An example of a freeze-substitution image is presented in Fig. 2(B).

This method is an improved version of a conventional one that consists in performing the following steps at room temperature: specimen chemical fixation, dehydration in organic solvents, embedding in resin or plastic, sectioning and

 

post-staining. The improvement is that the structure is better preserved since the artefacts caused by chemical fixation and dehydration at room temperature are avoided. However, the method based on freeze substitution is not completely free of artefacts (Dubochet & Sartori Blanc, 2001). Moreover, cryo-EM images of thin frozen-hydrated sections show differences with respect to the images of plastic sections obtained after high-pressure freezing and freeze substitution (Al-Amoudi *et al.*, 2004b).

Unfortunately, although the freeze-substitution method allows studies of whole cells and tissues and provides a good representation of membranous and larger supramolecular structures, it does not reach the resolution needed for a reliable interpretation at the molecular level mostly owing to radiation-induced distortions (Section 'Resolution').

Negative staining with heavy metal salts is often used for increasing the contrast in electron microscopy (Brenner & Horne, 1959). The heavy metals accumulate around the molecules of the specimen and also penetrate the cavities replacing water. Although the stain increases the contrast in images, it is not recommended for use in high-resolution structural studies because the images do not show faithfully the internal structure of biological material but only molecular surfaces accessible to the stain. However, staining can be useful in low-resolution studies aimed at obtaining an initial 3D model that can be further refined using high-resolution, unstained images.

Unlike the ET of stained plastic sections, cryo-ET of unstained cryo-sections has the potential to reach the resolution required for a reliable interpretation at the molecular level. Its broader use requires further development of methods for routinely cutting good-quality thin sections. A promising method for producing thin sections of frozen-hydrated specimens is focussed ion beam, which is commonly used in materials science to shape specimens for a variety of applications. It has been recently shown that focussed ion beam can be used for artefact-free thinning of whole frozen-hydrated cells, which leads to a successful reconstruction by cryo-ET (Marko *et al.*, 2007).

For further reading on specimen preservation techniques for ET, see Lucic *et al.* (2005) and McIntosh *et al.* (2005).

### *Automated acquisition*

Automation of electron microscopes started in the early 1990s (Dierksen *et al.*, 1992). Nowadays, robots automatically loading samples in the microscope are being developed (Potter *et al.*, 2004). Data-collection software for the microscope automatically surveys sample grids to select areas with appropriate ice thickness, autofocus and record images (Zheng *et al.*, 2004; Lei & Frank, 2005; Nickell *et al.*, 2005; Suloway *et al.*, 2005; Stagg *et al.*, 2006; Nickell *et al.*, 2007). One can also automatically monitor specimen tilt (Ziese *et al.*, 2003) or detect and discard images presenting defects such as charging, drift and absence of signal (Jonic *et al.*, 2007). The common goal of all these ongoing developments is to allow a quasi-automatic computation of a 3D map at sub-nanometer resolution within a day or two after inserting the specimen grid in the microscope (Zhu *et al.*, 2001). However, the acquisition is still mainly manual because these methods are not standard yet and especially because of difficulties in transferring specimen grids in the microscope in the case of cryo-techniques.

Regarding ET, the automation of data acquisition is indispensable for minimization of the exposure time. Since the same specimen is subjected to multiple exposures, the accumulated electron dose should be kept at a minimum. Ideally, the total time of a micrograph acquisition should be equal to the time of its recording. However, the recording is preceded by automated tracking and auto-focussing to compensate for the specimen lateral displacement and the displacement in the beam direction, respectively (Koster *et al.*, 1997; Rath *et al.*, 1997). They are performed on low-dose micrographs recorded at positions that are different from the final exposure position to minimize the received electron dose. Mechanical inaccuracies of the specimen holder are the main cause of the specimen movements during tilting, and ongoing development of procedures based upon a prediction of the specimen movement and highly stable specimen holders will lead to a faster acquisition under low-dose, cryo-conditions (Zheng *et al.*, 2004).

## Image processing

Imaging of a 3D object at different orientations using a static electron source and detector system is equivalent to imaging of a static 3D object using an electron source and detector system that rotate around the object. Thus, each 2D projection image acquired in an electron microscope corresponds to one projection direction in the equivalent system (Fig. 3). The reconstruction of an object from its 2D projection images acquired in the electron microscope is therefore usually performed in two steps. In the first step, the object is centred and aligned rotationally with respect to the principal axes in each of the object's individual experimental images, and the projection direction is determined for each of these images. In the second step, a volume is reconstructed using these images and their orientation and position parameters computed in the previous step.

For the reconstruction using SPA, a sufficient number of copies of the studied object has to be extracted from the acquired micrographs. Many algorithms have been developed for automatic particle selection and their extraction from micrographs (Nicholson & Glaeser, 2001; Zhu *et al.*, 2004).

### *Alignment for the first 3D model*

There are two types of techniques for determining the orientation and position of 2D projections in 3D space:

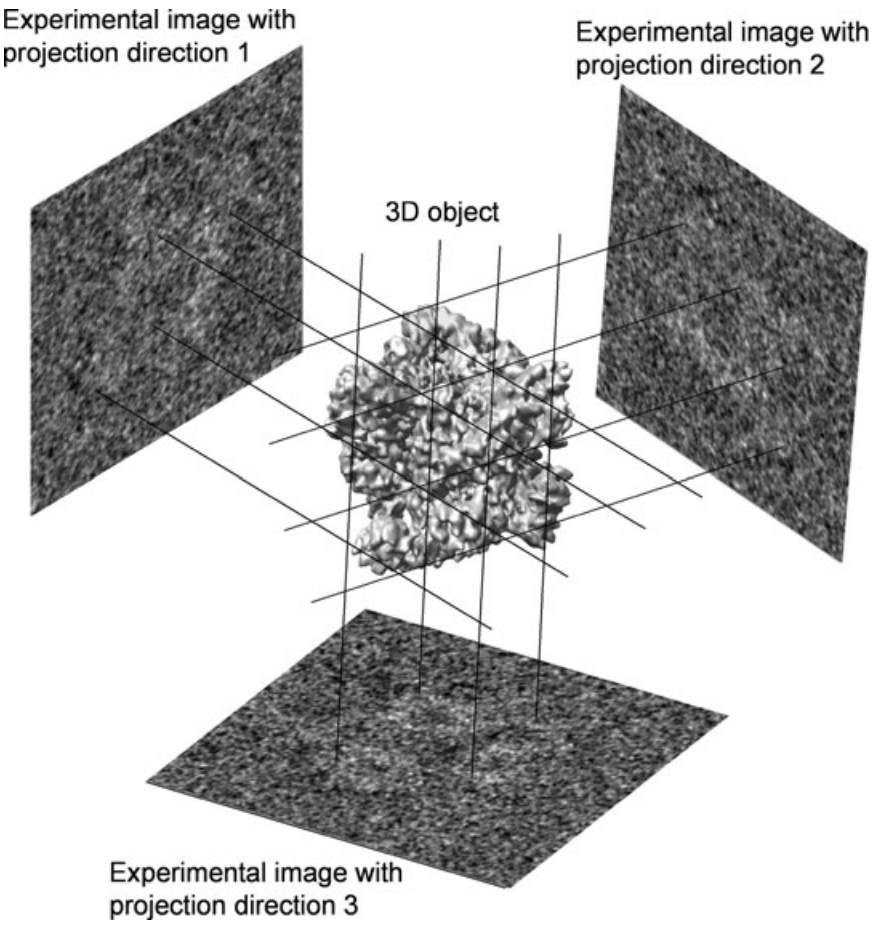


**Fig. 3.** Projection direction determination and 2D alignment for each of the object's individual experimental images. Imaging of a 3D object at different orientations using a static electron source and detector system is equivalent to imaging of a static 3D object using an electron source and detector system that rotate around the object. Thus, each 2D projection image acquired in an electron microscope corresponds to one projection direction in the equivalent system. The reconstruction of an object from its 2D projection images acquired in the electron microscope therefore requires prior centring and rotational alignment of the object in each of its individual experimental images as well as the determination of the projection direction for each of the experimental images. The figure shows a 3D object and experimental images corresponding to three arbitrarily chosen projection directions. The specimen is Glutamate synthase from Fig. 1.

reference-free and reference-based. Reference-free methods are used to determine the alignment parameters for computing a first, low-resolution 3D model since they do not require any reference 3D model. Reference-based methods require a reference 3D model and refine the alignment parameters iteratively to determine a high-resolution 3D model. Reference-free methods are discussed in this section, whereas reference-based methods will be discussed in the section 'Refinement of the alignment'.

In SPA, the orientation of each copy of the object has to be determined before starting the 3D reconstruction process. Two techniques are commonly used to determine the orientation of particles for the first 3D model: the method of *random conical tilt series* (Radermacher, 1988) and the techniques based on *common lines* (Crowther, 1971; van Heel, 1987; Goncharov, 1990; Penczek *et al.*, 1996). According to the method of random conical tilt series, each field is imaged twice (with the specimen holder tilted at 45° and 0°). The orientation of the tilted particles is determined from the known tilt geometry and the alignment and classification of the untilted particle images. These parameters are then used with the tilted particle images for the computation of a first 3D reconstruction volume. The techniques that use common lines generally require the classification of particle images and computation of class averages to reduce noise for a correct image alignment. Geometrical relationships between class averages are then computed using the relative orientation of their common lines, and a first 3D reconstruction volume is then computed using the determined orientation parameters and the class averages. Three different projections are at least required to orient images of an entirely asymmetric particle and to determine the enantiomorphic type of the 3D structure.

 

In ET, projection images share a common line that corresponds to the tilt axis. Therefore, the determination of the tilt axis is essential for an accurate 3D reconstruction. Ideally, the object does not move during image acquisition. In this ideal case, the orientation of the tilt axis would be found as a common line present in all power spectra of the specimen tilt series. However, in practice, one generally has to perform a translational and rotational alignment of the projection images to determine the orientation of the tilt axis because of drifts that occur during image acquisition. These drifts have a mechanical origin but may be coupled with charging effects or thermal drifts in the case of samples observed at liquid nitrogen temperature. The post-acquisition 2D alignment can be performed using methods based on cross-correlation or using recognizable features such as gold fiducial markers added to the sample (Guckenberger, 1982; Lawrence, 1992; Owen & Landis, 1996; Brandt *et al.*, 2001; Winkler & Taylor, 2006). Once the tilt series is aligned and the tilt parameters are determined, the 3D structure can be computed using any of the reconstruction methods described later.

*Reconstruction algorithms*

The most widely used families of reconstruction algorithms in 3D TEM are *direct Fourier inversion*, *backprojection* and *algebraic* methods. The *direct Fourier inversion* methods use the central slice theorem to assemble the 2D Fourier transforms of the experimental images within an estimated 3D Fourier transform of the object (Kak & Slaney, 1988; Grigorieff, 1998; Penczek *et al.*, 2004). Complicated interpolation schemes are required to compute the 3D Fourier transform on a regular grid (Lanzavecchia *et al.*, 1999; Penczek *et al.*, 2004). A 3D model of the object in real space is then obtained after the inverse 3D Fourier transformation.

*Backprojection methods* combine real-space experimental images in real 3D space to reconstruct a 3D object (Kak & Slaney, 1988). Simple linear real-space interpolation is usually sufficient in this case. Images are usually weighted before being summed in real 3D space to compensate for an uneven sampling in the reciprocal space (enhancement of low frequencies) (Harauz & van Heel, 1986; Radermacher *et al.*, 1986; Radermacher, 1992). This method is known as *weighted backprojection* and it is particularly suited to conical-tilt geometry (Radermacher, 1988).

*Algebraic methods* express the reconstruction volume in real space as a weighted sum of shifted basis functions (e.g., voxels, blobs) and then estimate the weights through a linear equation system (Herman, 1980). The most popular algebraic methods in 3D TEM are Block ART (for Algebraic Reconstruction Technique) (Gordon *et al.*, 1970; Marabini *et al.*, 1998) and SIRT (for Simultaneous Iterative Reconstruction Technique) (Gilbert, 1972; Penczek *et al.*, 1992). In the case of an uneven distribution of projection directions, it was shown that both weighted backprojection and algebraic methods produce elongations of the reconstructed volumes in the regions with the highest concentration of projection directions (Boisset *et al.*, 1998; Sorzano *et al.*, 2001). However, with the same data set, algebraic reconstruction methods with the proper selection of free parameters do not exhibit these elongations (Sorzano *et al.*, 2001).

*Refinement of the alignment*

Many iterative algorithms have been developed to refine orientation and position of particle images with respect to a reference volume. There are two types of these algorithms. Both estimate the alignment parameters for an experimental image by minimizing the dissimilarity between the experimental image and 2D projections of the reference volume (reference projections). The first type of algorithms samples the space of test angles and the space of test translations uniformly, and compares the experimental image with only those reference projections that were computed using a set of reference, uniformly sampled projection directions (Penczek *et al.*, 1994; Radermacher, 1994; Sorzano *et al.*, 2004b). In each iteration, a 3D reconstruction is computed from experimental images using the current alignment parameters, and this volume is used in the next iteration as a reference. The sampling step for the computation of reference projections is reduced gradually during the iterative refinement to improve the alignment accuracy. The smaller is the step, the more accurate is the alignment, but the slower is the determination of the alignment parameters.

The second type of refinement algorithms does not require a parameter such as a sampling step (Grigorieff, 1998; Jonic *et al.*, 2005; Grigorieff, 2007). Reference projections for comparison with experimental images are computed with orientation and position parameters determined by gradient-based optimization algorithms. These methods determine the alignment parameters in Fourier space using the central slice theorem. This means that they are fast but may require more complicated interpolation schemes than the first type of algorithms. Traditionally, the refinement is done using the first type of algorithms until the algorithm gets close to the solution. Then, to perform a fast refinement around the lastly computed alignment parameters, the refinement is continued using the second type of refinement algorithms.

*Software*

The most often used software packages for ET are open-source or freeware packages such as IMOD (Kremer *et al.*, 1996), TOM (Nickell *et al.*, 2005), TomoJ (Messaoudi *et al.*, 2007), EM (Hegerl, 1996) and UCSF tomography (Zheng *et al.*, 2007). As far as SPA is considered, the most often used general packages are open-source packages such as SPIDER (Frank *et al.*, 1996; Baxter *et al.*, 2007), Xmipp (Sorzano *et al.*, 2004a), EMAN (Ludtke *et al.*, 1999; Tang *et al.*, 2007), Bsoft (Heymann, 2001;

Heymann & Belnap, 2007) and SPARX (Hohn *et al.*, 2007), as well as the commercial package IMAGIC (van Heel *et al.*, 1996).

## Resolution

If microscopes were totally devoid of defects, their resolution would only be limited by the wavelength of the beam (Abbe, 1873). In this ideal case, even at 80 kV [the wavelength of 0.004 nm determining the theoretical limit of resolution of approximately 0.002 nm (Hawkes & Spence, 2007)], details as small as 0.002 nm could be reliably seen. However, such a high resolution is never achieved with 3D reconstruction practices. Other than the accuracy with which the individual images are aligned before the reconstruction and the accuracy of the reconstruction algorithm, many other practical factors limit the achievable resolution in practice. They will be discussed in this section as well as measurement of resolution.

### *Structure preservation*

Frozen-hydrated samples prepared by plunge freezing are likely to represent living cells because the sample is frozen within milliseconds and many of the cells will grow and divide when warmed rapidly to physiological temperatures (McIntosh, 2001). In high-pressure freezing, if the pressure is increased quickly and followed immediately by rapid freezing, the potentially damaging effects of high pressure are minimized and, as in plunge freezing, many frozen cells will live after thawing. However, once the freeze substitution takes place, the cells will not recover when warmed as all the water has been replaced by organic solvent.

Regarding the use of stain for contrast enhancement, the position of the stain might not accurately reflect the shapes of the macromolecules to which it binds. An additional problem encountered when using stain in ET is that the required electron dose can cause migration and agglomeration of the stain, which makes interpretation of the 3D reconstruction difficult.

### *Noise*

The noise in experimental images is mainly caused by an insufficient sampling of the electron scattering from the specimen and by imperfections of the image detector. Three-dimensional reconstruction acts as a low-pass filter, which reduces the noise in three dimensions. However, the 3D structure is to some extent still obscured by the noise, which limits the usable resolution. This is especially true in the case of volumes obtained by cryo-ET (cryo-tomograms), which have extremely low SNRs. The low SNR is usually increased using a filtering algorithm (Stoschek & Hegerl, 1997; Frangakis & Hegerl, 2001; Jiang *et al.*, 2003). These algorithms remove some noise but may, at the same time, remove a part of the signal. Denoising based on wavelet transforms preserves better the structural information (Stoschek & Hegerl, 1997).

### *Radiation damage*

Higher electron doses (e.g., greater than 10 electrons$Å^{-2}$ in a 200-kV microscope) produce less noisy images but damage the sample through ionization, breaking of chemical bonds and formation of free radicals, deteriorating thus the resolution.

At room temperature, for instance, in the case of plastic sections prepared using high-pressure freezing with freeze substitution, the most striking effect of radiation damage is the shrinkage of sections (40–50% in the direction of the beam and 5–10% in the plane perpendicular to it) owing to the loss of mass (Lucic *et al.*, 2005). This makes difficult an accurate 3D reconstruction and produces ambiguities in combining tomograms from neighbouring sections. Thus, an inaccurate representation of the native material due to preparation and beam-induced artefacts mainly limits the resolution achievable with this method.

The radiation damage at low temperatures causes a gradual deterioration of the achievable resolution, formation of bubbles of $H_2$ gas from decomposed water in the sample but no mass loss (Leapman & Sun, 1995; Lucic *et al.*, 2005). According to the *principle of dose fractionation*, the tolerable dose in ET should be divided among all tilt-series images; thus, the SNR of a tomogram is determined by the total dose for all images (McEwen *et al.*, 1995). The total dose received by the object should be kept as low as possible, which requires a fast and automatic data acquisition (Koster *et al.*, 1997). However, in practice, the dose per image is selected to be sufficient to produce enough detail in images for their accurate alignment.

### *Thickness of the sample*

With the thicker samples that take advantage of ET, the likelihood that a beam electron will interact more than once with the sample is increased. In this case, the image is no longer a simple projection of the sample, which means that image resolution is reduced, unless a specific correction is made. In the case of inelastic scattering, the incident electrons lose energy while transferring it to the sample. This causes damage to the sample (ionization and formation of free radicals), which also reduces image quality. The inelastic electron scattering contributes to the formation of the background noise in the electron diffraction pattern. Therefore, when imaging thicker samples, the contrast improvement is often done using a filter that removes most of the electrons having lost energy (*energy filtering*), which improves the SNR (Grimm *et al.*, 1996).

Only the smallest cells, the thinnest parts of cells and some isolated organelles are appropriate for ET without cutting the sample into slices of suitable thickness [200 nm or less for a

 

microscope at 200 kV, 400 nm or less at 300 kV and 500 nm or less at 1000 kV (McIntosh *et al.*, 2005)].

Resolution improvement in the case of thick samples will require improving the ability of CCD cameras to capture energetic electrons (e.g., 300 keV that work well for thicker specimens) and to better preserve structural information at high spatial frequencies (McIntosh *et al.*, 2005).

### *Contrast transfer function*

One of the factors limiting the resolution are imperfections of the electron microscope (spherical and chromatic aberrations, instabilities of magnetic lenses, instabilities of electron acceleration, additive noise, drift or charging etc.) that cause image deterioration (Frank, 2006a). Image formation with a majority of microscope imperfections is modeled by the *contrast transfer function* (CTF). The CTF is expressed in reciprocal space and its equivalent in real space is named *point spread function* as it describes how a single point is spread into a diffused spot when imaged in the microscope.

Many methods have been designed to correct the CTF computationally for SPA reconstruction. Each method comprises two steps. First, the parameters of a theoretical CTF model are estimated. This is done by minimizing a measure of dissimilarity between the experimental power spectrum density and its model (Zhou *et al.*, 1996; Huang *et al.*, 2003; Mindell & Grigorieff, 2003; Velazquez-Muriel *et al.*, 2003; Sorzano *et al.*, 2007b). Second, the CTF is corrected using the estimated parameters and one of the existing CTF correction methods (Typke *et al.*, 1992; Frank & Penczek, 1995; Penczek *et al.*, 1997; Sorzano *et al.*, 2004c). The most difficult part is definitely an accurate CTF estimation, knowing that images may have a very poor SNR, which is the case of low-dose cryo-electron micrographs.

The development of methods for a more accurate estimation and correction of the CTF is an old topic in SPA, although still attractive. However, the development of methods for CTF estimation and correction in ET started only recently. The interest to correct for the CTF in ET has arisen only when reconstructions approaching molecular resolutions started being obtained in practice. However, the CTF estimation methods used in SPA cannot be applied directly in ET because of different image acquisition geometries in the two cases. Theoretical modelling of the CTF in ET to take into account the tilt of the sample grid and the specimen thickness is a research in progress (Lawrence *et al.*, 2006; Philippsen *et al.*, 2007). The correction of the CTF will require its correct estimation from images using the theoretical CTF model. Currently, this seems to be a very difficult task, especially in the case of low-dose tilt-series images of non-stained, frozen-hydrated specimens because of a very low SNR. Further improvements in the CCD camera design that will allow a better detection of moderate- to high-resolution structural details and a reduced noise level in acquired images are necessary to permit the CTF estimation and correction and, thus, make possible reaching resolutions below 3 nm.

The majority of objects studied by electron microscopy and certainly all cryo-specimens are *phase objects*. A phase object does not absorb radiation (the outgoing wave has the same amplitude as the incoming wave), but rather delays or advances the incoming wave, leading to an object wave that locally has a phase different from that in the rest of the object plane. When recording images, the amplitude information (i.e., the square of the wave functions) is only recorded, whereas the phase information is lost. Thus, the image registered in an ideal microscope will not show the phases that we are most interested in, but rather just a homogeneous grey image. The phase information becomes visible after defocussing the microscope (causing the lenses to deviate from the focus). The electron microscope has an aberration (spherical aberration) that causes additional phase shifts in the back focal plane. Combining under-focus and spherical aberration, one manipulates the phases of the diffracted beams with respect to the zero-order beam such that they interfere constructively in the image plane. In this way, one optimizes the instrument to convert the phase variations in the object plane into amplitude variations in the image plane, which means that the amplitudes in the registered image contain the information about the phases, which is exactly what we are interested in.

Given the right combination of under-focus and spherical aberration, one obtains an almost ideal phase-contrast microscope for a large frequency range. Zernike proposed the use of a *phase plate* in the back focal plane of the microscope to obtain exactly the same optical situation but without manipulating under-focus and spherical aberration (Zernike, 1942). The phase plate changes the relative length of the optical path of the diffracted beams with respect to the zero-order beam such that an extra phase difference is introduced between the two, which causes their interference. When using phase plates, CTF correction is not required (Danev & Nagayama, 2001, 2008). The phase plates have been shown to preserve low-frequency signal components well, which results in the improvement of the image contrast (Danev & Nagayama, 2001, 2007). Because of the potential for contrast improvement, they may find more applications in the future in imaging thick samples as in the ET case.

### *Missing projection directions*

To determine the 3D structure of an object, one should collect its 2D projections from all possible directions. In ET practice, however, only a limited set of projections can be collected in the microscope because of specimen damage under the electron beam and to specimen tilt limitations in the microscope. Owing to the slab geometry of most specimens, the specimen appears thicker to electrons when increasing the tilt angle. A longer electron path through a thick sample than through a thin

 

sample (the two samples tilted at the same angle) means that high tilt is useful for thinner specimens but not for thicker ones. The limiting factor at higher tilt angles is the thickness of the grid bars and the geometry of specimen holders. Thus, the maximum tilt angle is limited at around 70° since the electrons could still penetrate the sample at higher angles, albeit at a lower probability. However, specimen holders with geometries that will allow recording of projection images over a full 360° tilt range are in development [e.g., cylindrically symmetric specimen holders (Barnard *et al.*, 1992)]. The consequences of being unable to acquire images from all directions are artefacts in the computed 3D structure. Thanks to the central slice theorem (DeRosier & Klug, 1968; Kak & Slaney, 1988), these artefacts can be explained by the empty regions in the 3D Fourier space in which no information about the specimen was recorded. A particular shape of the artefacts in the 3D Fourier space in the case of single tilt axis is a wedge, which corresponds to the wedge in which no information about the specimen was recorded owing to the maximum tilt angle limit (thus the name 'missing wedge' for this type of artefacts). The negative effects of the missing wedge can be partially overcome by using two (Penczek *et al.*, 1995; Mastronarde, 1997) or more tilt axes (Messaoudi *et al.*, 2006). Double-tilt axis geometry reduces the missing wedge artefact to a 'missing pyramid' artefact (Penczek *et al.*, 1995; Mastronarde, 1997).

When taking images without tilting the specimen grid, as is the case in SPA, it is theoretically possible to acquire images from all projection directions (an example of a projection image acquired with this type of data collection geometry is shown in Fig. 1(B)). However, in practice, there might be missing projection directions because some particles may adopt preferred orientations. Hence, particles presenting some strong hydrophobic areas might always present these surface areas at the air–water interface of cryo-EM specimen grids (e.g., mammalian chaperonin CCTP).

*Structural heterogeneity*

When studying the specimen using SPA, structural variability of the sample is very often the main factor limiting the resolution. Macromolecules with structural flexibility may adopt different conformations to perform different molecular functions. However, reconstruction algorithms assume that images come from a homogeneous population (identical copies of a macromolecule). Several methods have been developed to study structural heterogeneity. These methods either separate projections in homogeneous classes using multi-reference classification or multivariate statistical classification (van Heel & Frank, 1981; van Heel & Stoffler-Meilicke, 1985; Lata *et al.*, 2000; Heymann *et al.*, 2003; Heymann *et al.*, 2004), compute elastic geometric transformations between (pseudo)atomic coordinates of two provided 3D structural conformations (Tama *et al.*, 2004), explicitly estimate the structural variability present in projections (Penczek *et al.*, 2006b) and identify regions that are the most likely to vary from one image to another (Scheres *et al.*, 2007).

*Resolution measures*

Several measures of resolution of volumes reconstructed with SPA techniques have been proposed in the literature (Penczek, 2002; Unser *et al.*, 2005; van Heel & Schatz, 2005; Sousa & Grigorieff, 2007). The most used in practice are those based on the Fourier shell correlation (FSC) (Harauz & van Heel, 1986; van Heel & Schatz, 2005). It comprises a division of the experimental-image data set in two sub-sets, a reconstruction of one volume from each sub-set, and a computation of the correlation between the 3D Fourier transforms of the volumes over shells of frequencies in the 3D Fourier space. A good agreement at low frequencies is indicated by the FSC value close to 1. The FSC falls gradually down for higher frequencies, which indicates a poor agreement between the two volumes at these frequencies. The resolution is thus usually determined as the Fourier shell radius for which the FSC falls below 0.5 (Bottcher *et al.*, 1997), although the FSC thresholds other than 0.5 are also in use (Saxton & Baumeister, 1982; Orlova *et al.*, 1997; Rosenthal & Henderson, 2003; van Heel & Schatz, 2005). A reliable resolution measure is only obtained when the two half data sets are aligned against two independent reference structures. When the alignment of images is done against the same reference, the resolution is over-estimated because the alignment introduces a correlation between the noise components present in the images (Grigorieff, 2000). However, the alignment against two independent references is rarely done in practice.

Regarding ET, a theoretically achievable resolution can be obtained from the Crowther criterion (Crowther *et al.*, 1970). According to this criterion, the resolution is proportional to the size of the object in the direction of the electron beam and inversely proportional to the number of images in a tilt series used for the object reconstruction. This means that highest resolutions can be achieved with smallest objects and when using a large number of images. This criterion is only valid for spherical specimens and for constant tilt increment and, thus, has limited practical applications in ET. A practical use of this criterion is also limited by a poorly defined size of the object studied by ET (sub-cellular components have various sizes in a cell) and by a non-isotropic resolution due to a limited tilt-angle range (e.g., in single-axis tilt, the objects perpendicular to the plane defined by the direction of the electron beam and the tilt axis are almost not resolved; in double-axis tilt, the resolution is more isotropic because a smaller region in the 3D Fourier space remains uncovered by the projection data). Also, the resolution achievable in practice is affected by other factors that are not covered by this criterion (see above). The measures that are used in SPA to estimate the resolution of the reconstructed volumes can be directly applied to ET, although this is rarely done, mainly because of the anisotropy

 

of resolution of tomograms and a small number of images. Yet, specific resolution measures have been designed for ET, for instance, the one that allows assessment of the dependence of the resolution on the tilt angle by comparing experimental projection images with the corresponding projections of the tomogram (Cardone *et al.*, 2005). Currently, they are rarely used in practice, and the resolution is still usually estimated either from the position of the first zero of the CTF of projection images (an exact value of the defocus, which is maintained constant for all images in the tilt series, determines the position of the first zero of the oscillating CTF and, thus, the achievable resolution limit) or as the minimal distance between the points recognized to belong to two distinct objects.

### Examples of reconstructed structures

Despite the imperfections of currently existing ET and SPA methods, important information has been obtained about the structure and the underlying biological function of many macromolecular complexes, organelles, parts of cells and entire cells.

The structures obtained at highest sub-nanometer resolutions using SPA techniques are generally those of well-ordered assemblies with icosahedral symmetry (Bottcher *et al.*, 1997; Zhou *et al.*, 2000; Saban *et al.*, 2006; Jaalinoja *et al.*, 2007), although many macromolecular assemblies with lower symmetry (Ludtke *et al.*, 2004; Martin *et al.*, 2007) and with no internal symmetry (Gabashvili *et al.*, 2000; Golas *et al.*, 2003; Connell *et al.*, 2007) have been resolved at sub-nanometer or near-sub-nanometer resolutions. Interest is currently intense in understanding the molecular functions by structural analysis of trapped intermediate structural conformations (Saibil & Ranson, 2002; Grob *et al.*, 2006; Penczek *et al.*, 2006a; Tama & Brooks, 2006; Scheres *et al.*, 2007) and in interpreting 3D structures obtained using SPA by fitting with known atomic-resolution sub-unit structures (Jiang *et al.*, 2001; Chacon & Wriggers, 2002; Tama *et al.*, 2004).

Figures 1(B–D) show an application of cryo-EM and SPA methods to determine the 3D organization of the $(\alpha\beta)_6$ 1.2 MDa multi-enzymatic complex *Glutamate synthase* (GltS) from *Escherichia coli*. The GltS are found in bacteria, yeast and plants, where they form with glutamine synthetase an essential pathway for ammonia assimilation. The technique used to compute the 3D electron density map of the whole complex is described in Sorzano *et al.* (2007a) and the interactions and function of the GltS sub-units are discussed in Cottevieille *et al.* (2008). The structure was computed from low-dose cryo-EM images of a GltS sample on a holey carbon film vitrified by plunge freezing in liquid ethane (Fig. 1(B)). As the global shape of the GltS was unknown at the beginning, the random conical tilt series method was used to compute a first, low-resolution structure (Radermacher *et al.*, 1987). This first model was refined using iterative projection matching combined with the CTF correction by Wiener filtering of volumes from focal series (Penczek *et al.*, 1994, 1997) until the resolution stabilized at 9.5 Å. In each of the refinement iterations, the volume was symmetrized according to $D_3$ point-group symmetry, which became evident since the first low-resolution model was computed. The final reconstructed structure is shown in Fig. 1(C). The 3D structure of the $\alpha$ sub-unit was solved by X-ray crystallography at atomic resolution [PDB code: 1ea0 (Binda *et al.*, 2000)], whereas the 3D structure of the sub-unit $\beta$ was derived from a homologous enzyme [PDB code: 1h7w (Dobritzsch *et al.*, 2001)] by secondary structure prediction (Callebaut *et al.*, 1997). These atomic structures were then fitted in the 3D electron density map semi-automatically using Chimera (Goddard *et al.*, 2007; Fig. 1(D)). The interaction between sub-units were then studied in terms of contacts between the fitted structures (Cottevieille *et al.*, 2008).

ET of plastic sections allowed structural and functional studies of such cellular sub-structures as Golgi apparatus (Mogelsvang *et al.*, 2004), basal bodies (O'Toole *et al.*, 2003), spindle pole bodies (O'Toole *et al.*, 1999), active zone material at synapses (Harlow *et al.*, 2001), presynaptic vesicles (Lenzi *et al.*, 2002), desmosomes (He *et al.*, 2003), or cell plates (Segui-Simarro *et al.*, 2004).

Figures 2(B–D) show an application of ET of plastic sections to determine the 3D structural architecture of the mammalian Golgi from the pancreatic beta cell line, HIT-T15 [reproduced from Marsh (2005), with permission from Elsevier]. Immortalized HIT-T15 was prepared by high-pressure freezing and freeze substitution, followed by plastic embedding, and thick (400-nm) plastic sections were cut. Figure 2(B) shows 1 of 80 tilt-series images of a plastic section. One tilt series was collected for each of two tilt axes by imaging the specimen tilted over a range of $\pm 60^\circ$ in increments of $1.5^\circ$. Individual tilt-series images were first aligned with respect to each other by cross-correlation and were then more accurately aligned thanks to fiducial markers (10-nm colloidal gold) placed on the sample before image acquisition. One 3D reconstruction was computed for each of the two tilt series, and the two reconstructions were combined to produce a single, dual-axis tilt reconstruction. Figure 2(C) shows a slice extracted from the volume reconstructed at approximately 6-nm resolution. The same procedure was used to reconstruct 3D structures of additional 400-nm-thick sections to allow the study of a larger portion of the Golgi ribbon. The serial reconstructed volumes were mutually aligned and then combined to create a single, large volume (approximately $3.1 \times 3.2 \times 1.2$ $\mu$m). Visible structures in the Golgi region were then modelled (segmented), using the IMOD software package (Kremer *et al.*, 1996). Membranes were segmented by placing points along the bilayers, connecting the points with coloured line segments and building closed contours that delimited distinct membrane-bounded compartments and vesicles for each tomographic slice. The structure of segmented

objects was then studied as well as the relationships between the segmented objects and the surrounding objects (Fig. 2(D)).

Examples of structures solved by cryo-ET without cryo-sections are small cellular structures such as mitochondria (Nicastro *et al.*, 2000), axonemes (McEwen *et al.*, 2002), slime mould eukaryotic cells (Medalia *et al.*, 2002) and prokaryotic cells (Grimm *et al.*, 1998). However, through these examples, the potential of cryo-ET was recognized, especially, regarding identification of particular molecules in tomograms [e.g., ATP synthase (Nicastro *et al.*, 2000)].

Recent advances in the development of cryo-sectioning methods allowed more reliable cryo-ET studies of various organelles in frozen-hydrated skin and liver sections (Hsieh *et al.*, 2006; Masich *et al.*, 2006; Norlen *et al.*, 2007). Three-dimensional reconstruction of microtubules in their cellular context has shown that it was possible to achieve a similar resolution with cryo-ET of frozen-hydrated sections to that achievable with plunge-frozen samples (approximately 4 nm), despite the artefacts inherent in the sections (Bouchet-Marquis *et al.*, 2007). The latter example shows the power of tomograms from vitreous sections in allowing studies of macromolecular assemblies in their natural environment (Bouchet-Marquis *et al.*, 2007).

## Concluding remarks and perspectives: integrated approach to analysis of biological structural complexity

Neither of the two methods, SPA and ET, used alone can give a complete picture of complex structural organization of biological material. A multi-resolution approach in structural organization requires a multi-resolution approach for its analysis. This means that there is a need to integrate techniques specialized for different levels of detail (atoms, molecules, organelles and whole cells) (Frank *et al.*, 2002).

It has been shown that SPA can be used to compute volumes with resolution that is sufficient for tracing helices (Ludtke *et al.*, 2004; Saban *et al.*, 2006; Connell *et al.*, 2007). Moreover, this technique is the only one providing the structure of macromolecules that cannot be solved by other experimental techniques (e.g., electron crystallography, X-ray crystallography or nuclear magnetic resonance). When 3D atomic structures of the macromolecular sub-units are known [solved by an experimental technique or by structure prediction (Callebaut *et al.*, 1997; Baker & Sali, 2001)], this complementary information can be used to study the interactions between the sub-units, the way in which they assemble and their function in the macromolecule. To this goal, known atomic structures of the sub-units are fitted in the 3D structure obtained by SPA, and their relative position and orientation are analyzed (as in the SPA example shown in this paper, Fig. 1(D)). For a reliable interpretation of the results of fitting, the resolution of the SPA reconstruction should be sub-nanometer. The fitting may be rigid or may take into account macromolecular flexibility (Tama *et al.*, 2004; Velazquez-Muriel & Carazo, 2007). However, the fitting still requires human interaction because of a very different resolution of details in the two 3D structures, and development of fully automatic and reliable fitting methods is still in progress.

Regarding ET, the most important issue is the interpretation of computed tomographic volumes. The interpretation of tomograms at the ultra-structural level requires their decomposition into structural components (e.g., membranes or organelles). In the majority of cases, a manual assignment of features is usually preferred to available segmentation algorithms. The interpretation of tomograms at the molecular level consists in recognition (location) of *a priori* known molecular shapes (from a library of macromolecular structures obtained by X-ray crystallography, nuclear magnetic resonance, electron crystallography, SPA etc.) and requires their discrimination in the case of different species. The information on the spatial relationships between the mapped macromolecular structures within the cell complements the macromolecular information provided by other approaches.

A reliable localization of proteins in samples preserved using high-pressure freezing with freeze substitution will require advances in techniques for tagging specific macromolecules with markers that are visible by TEM (McIntosh *et al.*, 2005). Regarding cryo-ET, the labelling is a difficult task. Detection and identification of macromolecules in unlabelled tomograms can be done in a fully automated way using computational methods such as template matching (Frangakis *et al.*, 2002). To accurately recognize and discriminate molecules without labels, the resolution of reconstructed volumes should be in the range of 2–3 nm (Bohm *et al.*, 2000).

Therefore, there is an intense interest currently in developing new methods for cryo-ET (from sample preservation and sectioning to image processing) that will push the resolution towards the level of 2–3 nm. For example, combination of ET and SPA approaches has been shown to improve resolution in some cases. Hence, when the sample contains many identical copies of the same structure, particle volumes extracted from tomograms can be averaged (Walz *et al.*, 1997) or traditional SPA classification and averaging strategies can be used to average projection images from identical particles and, thus, improve the SNR and the resolution of the reconstructed volume [e.g., the approach used to study the 3D structure of nuclear pore complex (Stoffler *et al.*, 2003)]. However, these approaches require truly identical structures and not structures in different conformations. In addition, the signal in the individual images/volumes should be strong enough to allow an accurate image/volume alignment before averaging. The combined SPA and ET methods can also be used to generate sufficiently reliable initial models (from a relatively small number of macromolecular complexes) that could then be refined using traditional SPA approaches, using thousands of differently oriented individual particle images.

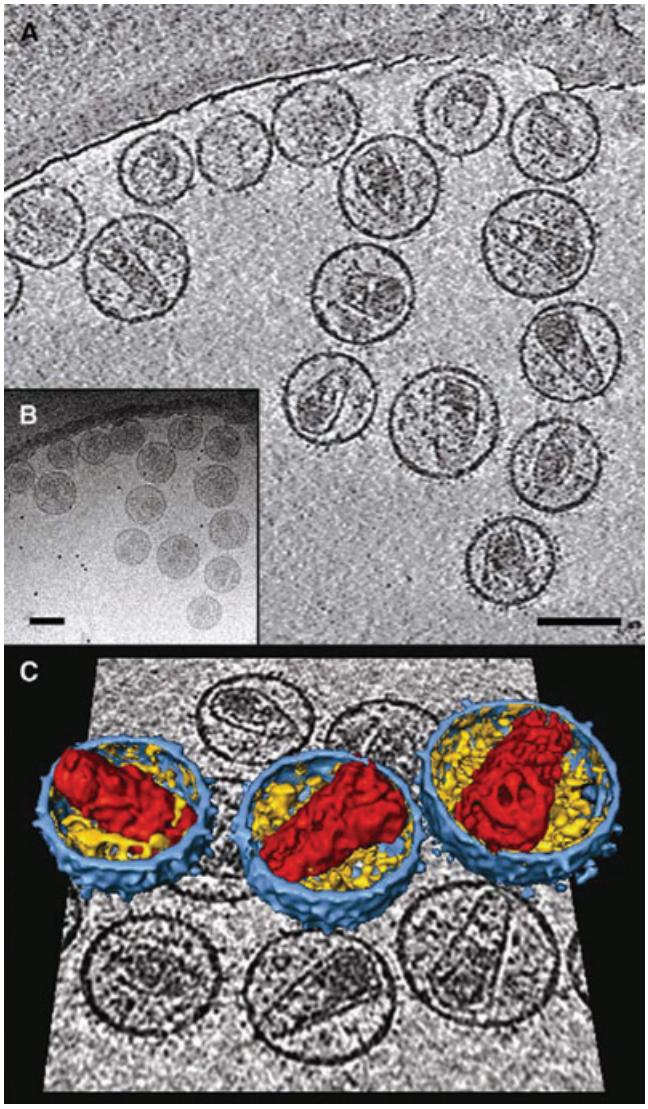


**Fig. 4.** Use of cryo-ET to reveal the heterogeneity of the core of HIV-1 virions in size and shape [reproduced from Briggs *et al.* (2006), with permission from Elsevier]. (A) Slice through the computed tomogram. HIV-1 particles were purified, inactivated, mixed with 10-nm colloidal gold and vitrified as described in Briggs *et al.* (2006). The virions have an approximately spherical shape, with diameters between 106 and 183 nm (Briggs *et al.*, 2006). (B) Projection image of the same area with visible gold fiducial markers. (C) Three-dimensional structure of three virions segmented from the tomogram shown above a central slice through it. Viral membrane, blue; density between the membrane and the core, yellow; viral capsid, red. The core was revealed by removing computationally half of the blue and yellow densities. The scale bars are 100 nm.

ET has a considerable potential for studying complexes with structural heterogeneity. For example, Fig. 4 shows the results of cryo-ET of a frozen-hydrated sample containing multiple copies of HIV-1 virions heterogeneous in size and shape [reproduced from Briggs *et al.* (2006), with permission from Elsevier]. This technique allowed the study of the diameter of the entire 3D virion structure and 3D morphology of the viral core of segmented virions. The virions were of an approximately spherical shape, with diameters between 106 and 183 nm, and of the 75 observed particles, 5 contained no well-defined core, 63 contained a single core, 3 contained 1 complete and 1 partial or indistinct core and 4 contained 2 cores (Briggs *et al.*, 2006).

In the future, following the same principle of multi-resolution analysis of biological complexity, one might take advantage of integrating volumes from ET into even lower-resolution volumes representing whole large cells without sectioning, obtained from X-ray tomography (Le Gros *et al.*, 2005) or even optical microscopy.

An extension of ET is its combination with chemical mapping by electron energy-loss spectroscopy that allows spatial localization of chemical components. It is already a well-established method in material sciences (Mobus *et al.*, 2003; Gass *et al.*, 2006) and is starting to be used in biology (Leapman *et al.*, 2004).

A routine combination of TEM data with data obtained with other methods will be an important future goal, which is already giving rise to new fields such as correlative light–electron microscopy (Leapman, 2004). It consists in combining light microscopy with ET for an efficient location of a sub-micrometre object on a grid of few millimetres under low-dose conditions. Light microscope can be used to locate an approximate position of the object using molecules with fluorescent labels or by identifying large features that are visible in the light microscope. The located region is then zoomed. However, further technological developments are required for a routine use of this method.

## Acknowledgements

We are grateful to European Commission for NoE '3D-EM' contract no. LSHG-CT-2004-502828, Region Ile-de-France for convention SESAME 2000 E 1435, program C'Nano Ile-de-France for supporting 3D cryo-EM at IMPMC.

## References

Abbe, E. (1873) Beitrage zur Theorie des Mikroskops und der Mikroskopischen Wahrnehmung. *Arch. Mikrosk. Anatomie*. **9**, 413–468.

Al-Amoudi, A., Chang, J.J., Leforestier, A., *et al.* (2004a) Cryo-electron microscopy of vitreous sections. *EMBO J.* **23**, 3583–3588.

Al-Amoudi, A., Norlen, L.P. & Dubochet, J. (2004b) Cryo-electron microscopy of vitreous sections of native biological cells and tissues. *J. Struct. Biol.* **148**, 131–135.

Baker, D. & Sali, A. (2001) Protein structure prediction and structural genomics. *Science* **294**, 93–96.

Baker, T.S., Olson, N.H. & Fuller, S.D. (1999) Adding the third dimension to virus life cycles: three-dimensional reconstruction of icosahedral viruses from cryo-electron micrographs. *Microbiol. Mol. Biol.* **63**, 862–922.

Barnard, D.P., Turner, J.N., Frank, J. & McEwen, B.F. (1992) A 360 degrees single-axis tilt stage for the high-voltage electron microscope. *J. Microsc.* **167**, 39–48.

Baxter, W.T., Leith, A. & Frank, J. (2007) SPIRE: the SPIDER reconstruction engine. *J. Struct. Biol.* **157**, 56–63.

Binda, C., Bossi, R.T., Wakatsuki, S., *et al.* (2000) Cross-talk and ammonia channeling between active centers in the unexpected domain arrangement of glutamate synthase. *Structure* **8**, 1299–1308.

Bohm, J., Frangakis, A.S., Hegerl, R., Nickell, S., Typke, D. & Baumeister, W. (2000) Toward detecting and identifying macromolecules in a cellular context: template matching applied to electron tomograms. *Proc. Natl. Acad. Sci. U.S.A.* **97**, 14245–14250.

Boisset, N., Penczek, P.A., Taveau, J.C., You, V., de Haas, F. & Lamy, J. (1998) Overabundant single-particle electron microscope views induce a three-dimensional reconstruction artifact. *Ultramicroscopy* **74**, 201–207.

Bottcher, B., Wynne, S.A. & Crowther, R.A. (1997) Determination of the fold of the core protein of hepatitis B virus by electron cryomicroscopy. *Nature* **386**, 88–91.

Bouchet-Marquis, C., Zuber, B., Glynn, A.M., *et al.* (2007) Visualization of cell microtubules in their native state. *Biol. Cell.* **99**, 45–53.

Brandt, S., Heikkonen, J. & Engehardt, P. (2001) Multiphase method for automatic alignment of transmission electron microscope images using markers. *J. Struct. Biol.* **133**, 10–22.

Brenner, S. & Horne, R.W. (1959) A negative staining method for high resolution electron microscopy of viruses. *Biochim. Biophys. Acta* **34**, 103–110.

Briggs, J.A., Grunewald, K., Glass, B., Forster, F., Krausslich, H.G. & Fuller, S.D. (2006) The mechanism of HIV-1 core assembly: insights from three-dimensional reconstructions of authentic virions. *Structure* **14**, 15–20.

Callebaut, I., Labesse, G., Durand, P., *et al.* (1997) Deciphering protein sequence information through hydrophobic cluster analysis (HCA): current status and perspectives. *Cell. Mol. Life Sci.* **53**, 621–645.

Cardone, G., Grunewald, K. & Steven, A.C. (2005) A resolution criterion for electron tomography based on cross-validation. *J. Struct. Biol.* **151**, 117–129.

Carragher, B., Whittaker, M. & Milligan, R.A. (1996) Helical processing using PHOELIX. *J. Struct. Biol.* **116**, 107–112.

Chacon, P. & Wriggers, W. (2002) Multi-resolution contour-based fitting of macromolecular structures. *J. Mol. Biol.* **317**, 375–384.

Comolli, L.R., Kundmann, M. & Downing, K.H. (2006) Characterization of intact subcellular bodies in whole bacteria by cryo-electron tomography and spectroscopic imaging. *J. Microsc.* **223**, 40–52.

Connell, S.R., Takemoto, C., Wilson, D.N., *et al.* (2007) Structural basis for interaction of the ribosome with the switch regions of GTP-bound elongation factors. *Mol. Cell.* **25**, 751–764.

Conway, J.F. & Steven, A.C. (1999) Methods for reconstructing density maps of "single" particles from cryoelectron micrographs to subnanometer resolution. *J. Struct. Biol.* **128**, 106–118.

Cottevieille, M., Larquet, E., Jonic, S., *et al.* (2008) The subnanometer resolution structure of the glutamate synthase 1.2 MDa hexamer by cryoelectron microscopy and its oligomerization behavior in solution: functional implications. *J. Biol. Chem.* **283**, 8237–8249.

Crowther, R.A. (1971) Procedures for three-dimensional reconstruction of spherical viruses by Fourier synthesis from electron micrographs. *Philos. Trans. R. Soc. Lond. B. Biol. Sci.* **261**, 221–230.

Crowther, R.A., DeRosier, D.J. & Klug, F.R.S. (1970) The reconstruction of a three-dimensional structure from projections and its application to electron microscopy. *Proc. R. Soc. Lond. A.* **317**, 310–340.

Cyrklaff, M., Risco, C., Fernandez, J.J., Jimenez, M.V., Esteban, M., Baumeister, W. & Carrascosa, J.L. (2005) Cryo-electron tomography of vaccinia virus. *Proc. Natl. Acad. Sci. U.S.A.* **102**, 2772–2777.

Danev, R. & Nagayama, K. (2001) Transmission electron microscopy with Zernike phase plate. *Ultramicroscopy* **88**, 243–252.

Danev, R. & Nagayama, K. (2008) Single particle analysis based on Zernike phase contrast transmission electron microscopy. *J. Struct. Biol.* **161**, 211–218.

DeRosier, D.J. & Klug, A. (1968) Reconstruction of three dimensional structures from electron micrographs. *Nature* **217**, 130–134.

DeRosier, D.J. & Moore, P.B. (1970) Reconstruction of three-dimensional images from electron micrographs of structures with helical symmetry. *J. Mol. Biol.* **52**, 355–369.

Dierksen, K., Typke, D., Hegerl, R., Koster, A.J. & Baumeister, W. (1992) Towards automatic electron tomography. *Ultramicroscopy* **40**, 71–87.

Dobritzsch, D., Schneider, G., Schnackerz, K.D. & Lindqvist, Y. (2001) Crystal structure of dihydropyrimidine dehydrogenase, a major determinant of the pharmacokinetics of the anti-cancer drug 5-fluorouracil. *EMBO J.* **20**, 650–660.

Donohoe, B.S., Mogelsvang, S. & Staehelin, L.A. (2006) Electron tomography of ER, Golgi and related membrane systems. *Methods* **39**, 154–162.

Dubochet, J., Adrian, M., Chang, J.J., Homo, J.C., Lepault, J., McDowall, A.W. & Schultz, P. (1988) Cryo-electron microscopy of vitrified specimens. *Q. Rev. Biophys.* **21**, 129–228.

Dubochet, J. & Sartori Blanc, N. (2001) The cell in absence of aggregation artifacts. *Micron* **32**, 91–99.

Egelman, E.H. (2007) The iterative helical real space reconstruction method: surmounting the problems posed by real polymers. *J. Struct. Biol.* **157**, 83–94.

Ellis, M.J. & Hebert, H. (2001) Structure analysis of soluble proteins using electron crystallography. *Micron* **32**, 541–550.

Falke, S., Tama, F., Brooks, C.L., 3rd, Gogol, E.P. & Fisher, M.T. (2005) The 13 angstroms structure of a chaperonin GroEL-protein substrate complex by cryo-electron microscopy. *J. Mol. Biol.* **348**, 219–230.

Fotin, A., Kirchhausen, T., Grigorieff, N., Harrison, S.C., Walz, T. & Cheng, Y. (2006) Structure determination of clathrin coats to subnanometer resolution by single particle cryo-electron microscopy. *J. Struct. Biol.* **156**, 453–460.

Frangakis, A.S., Bohm, J., Forster, F., *et al.* (2002) Identification of macromolecular complexes in cryoelectron tomograms of phantom cells. *Proc. Natl. Acad. Sci. U.S.A.* **99**, 14153–14158.

Frangakis, A.S. & Hegerl, R. (2001) Noise reduction in electron tomographic reconstructions using nonlinear anisotropic diffusion. *J. Struct. Biol.* **135**, 239–250.

Frank, J. (2002) Single-particle imaging of macromolecules by cryo-electron microscopy. *Annu. Rev. Biophys. Biomol. Struct.* **31**, 303–319.

Frank, J. (2006a) *Three-Dimensional Electron Microscopy of Macromolecular Assemblies: Visualization of Biological Molecules in Their Native State*. Oxford University Press, New York.

Frank, J. (2006b) *Electron Tomography: Methods for Three-Dimensional Visualization of Structures in the Cell*, 2nd edn. Springer, New York.

Frank, J. & Penczek, P.A. (1995) On the correction of the contrast transfer function in biological electron microscopy. *Optik* **98**, 125–129.

Frank, J., Radermacher, M., Penczek, P., Zhu, J., Li, Y., Ladjadj, M. & Leith, A. (1996) SPIDER and WEB: processing and visualization of images in 3D electron microscopy and related fields. *J. Struct. Biol.* **116**, 190–199.

 

Frank, J., Wagenknecht, T., McEwen, B.F., Marko, M., Hsieh, C.-E. & Mannella, C.A. (2002) Three-dimensional imaging of biological complexity. *J. Struct. Biol.* **138**, 85–91.

Gabashvili, I.S., Agrawal, R.K., Spahn, C.M., Grassucci, R.A., Svergun, D.I., Frank, J. & Penczek, P. (2000) Solution structure of the *E. coli* 70S ribosome at 11.5 Å resolution. *Cell* **100**, 537–549.

Gass, M.H., Koziol, K.K., Windle, A.H. & Midgley, P.A. (2006) Four-dimensional spectral tomography of carbonaceous nanocomposites. *Nano Lett.* **6**, 376–379.

Gilbert, P. (1972) Iterative methods for the three-dimensional reconstruction of an object from projections. *J. Theor. Biol.* **36**, 105–117.

Glaeser, R.M. (1971) Limitations to significant information in biological electron microscopy as a result of radiation damage. *J. Ultrastruct. Res.* **36**, 466–482.

Glaeser, R.M. (1999) Review: electron crystallography: present excitement, a nod to the past, anticipating the future. *J. Struct. Biol.* **128**, 3–14.

Goddard, T.D., Huang, C.C. & Ferrin, T.E. (2007) Visualizing density maps with UCSF Chimera. *J. Struct. Biol.* **157**, 281–287.

Golas, M.M., Sander, B., Will, C.L., Luhrmann, R. & Stark, H. (2003) Molecular architecture of the multiprotein splicing factor SF3b. *Science* **300**, 980–984.

Goncharov, A.B. (1990) Three-dimensional reconstruction of arbitrarily arranged identical particles given their projections. *Transl. Math. Monographs.* **81**, 67–95.

Gordon, R., Bender, R. & Herman, G.T. (1970) Algebraic reconstruction techniques (ART) for three-dimensional electron microscopy and X-ray photography. *J. Theor. Biol.* **29**, 471–481.

Grigorieff, N. (1998) Three-dimensional structure of bovine NADH:ubiquinone oxidoreductase (complex I) at 22 Å in ice. *J. Mol. Biol.* **277**, 1033–1046.

Grigorieff, N. (2000) Resolution measurement in structures derived from single particles. *Acta Crystallogr. D Biol. Crystallogr.* **56**(Pt 10), 1270–1277.

Grigorieff, N. (2007) FREALIGN: high-resolution refinement of single particle structures. *J. Struct. Biol.* **157**, 117–125.

Grimm, R., Koster, A.J., Ziese, U., Typke, D. & Baumeister, W. (1996) Zero-loss energy filtering under low-dose conditions using a post-column energy filter. *J. Microsc.* **183**, 60–68.

Grimm, R., Singh, H., Rachel, R., Typke, D., Zillig, W. & Baumeister, W. (1998) Electron tomography of ice-embedded prokaryotic cells. *Biophys. J.* **74**, 1031–1042.

Grob, P., Cruse, M.J., Inouye, C., Peris, M., Penczek, P.A., Tjian, R. & Nogales, E. (2006) Cryo-electron microscopy studies of human TFIID: conformational breathing in the integration of gene regulatory cues. *Structure* **14**, 511–520.

Grunewald, K., Desai, P., Winkler, D.C., Heymann, J.B., Belnap, D.M., Baumeister, W. & Steven, A.C. (2003) Three-dimensional structure of herpes simplex virus from cryo-electron tomography. *Science* **302**, 1396–1398.

Guckenberger, R. (1982) Determination of a common origin in the micrographs of tilt series in three-dimensional electron microscopy. *Ultramicroscopy* **9**, 167–174.

Harauz, G. & van Heel, M. (1986) Exact filters for general geometry three dimensional reconstruction. *Optik* **73**, 146–156.

Harlow, M.L., Ress, D., Stoschek, A., Marshall, R.M. & McMahan, U.J. (2001) The architecture of active zone material at the frog's neuromuscular junction. *Nature* **409**, 479–484.

Hawkes, P.W. & Spence, J.C.H. (2007) *Science of Microscopy*. Springer, New York.

Hayward, S.B. & Glaeser, R.M. (1979) Radiation damage of purple membrane at low temperature. *Ultramicroscopy* **4**, 201–210.

He, W., Cowin, P. & Stokes, D.L. (2003) Untangling desmosomal knots with electron tomography. *Science* **302**, 109–113.

Hegerl, R. (1996) The EM program package: a platform for image processing in biological electron microscopy. *J. Struct. Biol.* **116**, 30–34.

Herman, G.T. (1980) *Image Reconstruction from Projections: The Fundamentals of Computerized Tomography*. Academic Press, New York.

Heymann, J.B. (2001) Bsoft: image and molecular processing in electron microscopy. *J. Struct. Biol.* **133**, 156–169.

Heymann, J.B. & Belnap, D.M. (2007) Bsoft: image processing and molecular modeling for electron microscopy. *J. Struct. Biol.* **157**, 3–18.

Heymann, J.B., Cheng, N., Newcomb, W.W., Trus, B.L., Brown, J.C. & Steven, A.C. (2003) Dynamics of herpes simplex virus capsid maturation visualized by time-lapse cryo-electron microscopy. *Nat. Struct. Biol.* **10**, 334–341.

Heymann, J.B., Conway, J.F. & Steven, A.C. (2004) Molecular dynamics of protein complexes from four-dimensional cryo-electron microscopy. *J. Struct. Biol.* **147**, 291–301.

Hite, R.K., Raunser, S. & Walz, T. (2007) Revival of electron crystallography. *Curr. Opin. Struct. Biol.* **17**, 389–395.

Hohn, M., Tang, G., Goodyear, G., *et al.* (2007) SPARX, a new environment for cryo-EM image processing. *J. Struct. Biol.* **157**, 47–55.

Hsieh, C.E., Leith, A., Mannella, C.A., Frank, J. & Marko, M. (2006) Towards high-resolution three-dimensional imaging of native mammalian tissue: electron tomography of frozen-hydrated rat liver sections. *J. Struct. Biol.* **153**, 1–13.

Huang, Z., Baldwin, P.R., Mullapudi, S. & Penczek, P.A. (2003) Automated determination of parameters describing power spectra of micrograph images in electron microscopy. *J. Struct. Biol.* **144**, 79–94.

Jaalinoja, H.T., Huiskonen, J.T. & Butcher, S.J. (2007) Electron cryomicroscopy comparison of the architectures of the enveloped bacteriophages phi6 and phi8. *Structure* **15**, 157–167.

Jiang, W., Baker, M.L., Ludtke, S.J. & Chiu, W. (2001) Bridging the information gap: computational tools for intermediate resolution structure interpretation. *J. Mol. Biol.* **308**, 1033–1044.

Jiang, W., Baker, M.L., Wu, Q., Bajaj, C. & Chiu, W. (2003) Applications of a bilateral denoising filter in biological electron microscopy. *J. Struct. Biol.* **144**, 114–122.

Jonic, S., Sorzano, C.O., Cottevieille, M., Larquet, E. & Boisset, N. (2007) A novel method for improvement of visualization of power spectra for sorting cryo-electron micrographs and their local areas. *J. Struct. Biol.* **157**, 156–167.

Jonic, S., Sorzano, C.O., Thevenaz, P., El-Bez, C., De Carlo, S. & Unser, M. (2005) Spline-based image-to-volume registration for three-dimensional electron microscopy. *Ultramicroscopy* **103**, 303–317.

Kak, A.C. & Slaney, M. (1988) *Principles of Computed Tomographic Imaging*. IEEE Press, New York.

Kellenberger, E. (1991) The potential of cryofixation and freeze substitution: observations and theoretical considerations. *J. Microsc.* **161**, 183–203.

Koster, A.J., Grimm, R., Typke, D., Hegerl, R., Stoschek, A., Walz, J. & Baumeister, W. (1997) Perspectives of molecular and cellular electron tomography. *J. Struct. Biol.* **120**, 276–308.

Koster, A.J. & Klumperman, J. (2003) Electron microscopy in cell biology: integrating structure and function. *Nat. Cell Biol. Suppl. S*, SS6–SS10.

Kremer, J.R., Mastronarde, D.N. & McIntosh, J.R. (1996) Computer visualization of three-dimensional image data using IMOD. *J. Struct. Biol.* **116**, 71–76.

Lanzavecchia, S., Bellon, P.L. & Radermacher, M. (1999) Fast and accurate three-dimensional reconstruction from projections with random orientations via Radon transform. *J. Struct. Biol.* **128**, 152–164.

Lata, R., Conway, J.F., Cheng, N., *et al.* (2000) Maturation dynamics of a viral capsid: visualization of transitional intermediate states. *Cell* **100**, 253–263.

Lawrence, A., Bouwer, J.C., Perkins, G. & Ellisman, M.H. (2006) Transform-based backprojection for volume reconstruction of large format electron microscope tilt series. *J. Struct. Biol.* **154**, 144–167.

Lawrence, M.C. (1992) Least-squares method of alignment using markers. *Electron Tomography* (ed. by J. Frank), pp. 197–204. Plenum Press, New York.

Le Gros, M.A., McDermott, G. & Larabell, C.A. (2005) X-ray tomography of whole cells. *Curr. Opin. Struct. Biol.* **15**, 593–600.

Leapman, R.D. (2004) Novel techniques in electron microscopy. *Curr. Opin. Neurobiol.* **14**, 591–598.

Leapman, R.D., Kocsis, E., Zhang, G., Talbot, T.L. & Laquerriere, P. (2004) Three-dimensional distributions of elements in biological samples by energy-filtered electron tomography. *Ultramicroscopy* **100**, 115–125.

Leapman, R.D. & Sun, S. (1995) Cryo-electron energy loss spectroscopy: observations on vitrified hydrated specimens and radiation damage. *Ultramicroscopy* **59**, 71–79.

Lei, J. & Frank, J. (2005) Automated acquisition of cryo-electron micrographs for single particle reconstruction on an FEI Tecnai electron microscope. *J. Struct. Biol.* **150**, 69–80.

Lenzi, D., Crum, J., Ellisman, M.H. & Roberts, W.M. (2002) Depolarization redistributes synaptic membrane and creates a gradient of vesicles on the synaptic body at a ribbon synapse. *Neuron* **36**, 649–659.

Lucic, V., Forster, F. & Baumeister, W. (2005) Structural studies by electron tomography: from cells to molecules. *Annu. Rev. Biochem.* **74**, 833–865.

Ludtke, S.J., Baldwin, P.R. & Chiu, W. (1999) EMAN: semiautomated software for high-resolution single-particle reconstructions. *J. Struct. Biol.* **128**, 82–97.

Ludtke, S.J., Chen, D.H., Song, J.L., Chuang, D.T. & Chiu, W. (2004) Seeing GroEL at 6 Å resolution by single particle electron cryomicroscopy. *Structure* **12**, 1129–1136.

McEwen, B.F., Downing, K.H. & Glaeser, R.M. (1995) The relevance of dose-fractionation in tomography of radiation-sensitive specimens. *Ultramicroscopy* **60**, 357–373.

McEwen, B.F., Marko, M., Hsieh, C.E. & Mannella, C. (2002) Use of frozen-hydrated axonemes to assess imaging parameters and resolution limits in cryoelectron tomography. *J. Struct. Biol.* **138**, 47–57.

McIntosh, J.R. (2001) Electron microscopy of cells: a new beginning for a new century. *J. Cell Biol.* **153**, F25–F32.

McIntosh, R., Nicastro, D. & Mastronarde, D. (2005) New views of cells in 3D: an introduction to electron tomography. *Trends Cell Biol.* **15**, 43–51.

Marabini, R., Herman, G.T. & Carazo, J.M. (1998) 3D reconstruction in electron microscopy using ART with smooth spherically symmetric volume elements (blobs). *Ultramicroscopy* **72**, 53–65.

Marko, M., Hsieh, C., Schalek, R., Frank, J. & Mannella, C. (2007) Focused-ion-beam thinning of frozen-hydrated biological specimens for cryo-electron microscopy. *Nat. Methods* **4**, 215–217.

Marsh, B.J. (2005) Lessons from tomographic studies of the mammalian Golgi. *Biochim. Biophys. Acta* **1744**, 273–292.

Martin, A.G., Depoix, F., Stohr, M., *et al.* (2007) Limulus polyphemus hemocyanin: 10 Å cryo-EM structure, sequence analysis, molecular modelling and rigid-body fitting reveal the interfaces between the eight hexamers. *J. Mol. Biol.* **366**, 1332–1350.

Masich, S., Ostberg, T., Norlen, L., Shupliakov, O. & Daneholt, B. (2006) A procedure to deposit fiducial markers on vitreous cryo-sections for cellular tomography. *J. Struct. Biol.* **156**, 461–468.

Mastronarde, D.N. (1997) Dual-axis tomography: an approach with alignment methods that preserve resolution. *J. Struct. Biol.* **120**, 343–352.

Medalia, O., Weber, I., Frangakis, A.S., Nicastro, D., Gerisch, G. & Baumeister, W. (2002) Macromolecular architecture in eukaryotic cells visualized by cryoelectron tomography. *Science* **298**, 1209–1213.

Messaoudi, C., Boudier, T., Sanchez Sorzano, C.O. & Marco, S. (2007) TomoJ: tomography software for three-dimensional reconstruction in transmission electron microscopy. *BMC Bioinform.* **8**, 288.

Messaoudi, C., Loubresse, N.G.d., Boudier, T., Dupuis-Williams, P. & Marco, S. (2006) Multiple-axis tomography: applications to basal bodies from paramecium tetraurelia. *Biol. Cell.* **98**, 415–425.

Mindell, J.A. & Grigorieff, N. (2003) Accurate determination of local defocus and specimen tilt in electron microscopy. *J. Struct. Biol.* **142**, 334–347.

Mobus, G., Doole, R.C. & Inkson, B.J. (2003) Spectroscopic electron tomography. *Ultramicroscopy* **96**, 433–451.

Mogelsvang, S., Marsh, B.J., Ladinsky, M.S. & Howell, K.E. (2004) Predicting function from structure: 3D structure studies of the mammalian Golgi complex. *Traffic* **5**, 338–345.

Morgan, D.G. & Rosier, D.J.D. (1992) Processing images of helical structures: a new twist. *Ultramicroscopy* **46**, 263–285.

Navaza, J. (2003) On the three-dimensional reconstruction of icosahedral particles. *J. Struct. Biol.* **144**, 13–23.

Nicastro, D., Frangakis, A.S., Typke, D. & Baumeister, W. (2000) Cryo-electron tomography of neurospora mitochondria. *J. Struct. Biol.* **129**, 48–56.

Nicholson, W.V. & Glaeser, R.M. (2001) Review: automatic particle detection in electron microscopy. *J. Struct. Biol.* **133**, 90–101.

Nickell, S., Beck, F., Korinek, A., Mihalache, O., Baumeister, W. & Plitzko, J.M. (2007) Automated cryoelectron microscopy of "single particles" applied to the 26S proteasome. *FEBS Lett.* **581**, 2751–2756.

Nickell, S., Forster, F., Linaroudis, A., *et al.* (2005) TOM software toolbox: acquisition and analysis for electron tomography. *J. Struct. Biol.* **149**, 227–234.

Norlen, L., Masich, S., Goldie, K.N. & Hoenger, A. (2007) Structural analysis of vimentin and keratin intermediate filaments by cryo-electron tomography. *Exp. Cell Res.* **313**, 2217–2227.

O'Toole, E.T., Giddings, T.H., McIntosh, J.R. & Dutcher, S.K. (2003) Three-dimensional organization of basal bodies from wild-type and delta-tubulin deletion strains of *Chlamydomonas reinhardtii*. *Mol. Biol. Cell.* **14**, 2999–3012.

O'Toole, E.T., Winey, M. & McIntosh, J.R. (1999) High-voltage electron tomography of spindle pole bodies and early mitotic spindles in the yeast *Saccharomyces cerevisiae*. *Mol. Biol. Cell.* **10**, 2017–2031.

O'Toole, E.T., Winey, M., McIntosh, J.R. & Mastronarde, D.N. (2002) Electron tomography of yeast cells. *Methods Enzymol.* **351**, 81–95.

Orlova, E.V., Dube, P., Harris, J.R., Beckman, E., Zemlin, F., Markl, J. & van Heel, M. (1997) Structure of keyhole limpet hemocyanin type 1

 

(KLH1) at 15 Å resolution by electron cryomicroscopy and angular reconstitution. *J. Mol. Biol.* **271**, 417–437.

Owen, C.H. & Landis, W.J. (1996) Alignment of electron tomographic series by correlation without the use of gold particles. *Ultramicroscopy* **63**, 27–38.

Penczek, P., Marko, M., Buttle, K. & Frank, J. (1995) Double-tilt electron tomography. *Ultramicroscopy* **60**, 393–410.

Penczek, P., Radermacher, M. & Frank, J. (1992) Three-dimensional reconstruction of single particles embedded in ice. *Ultramicroscopy* **40**, 33–53.

Penczek, P.A. (2002) Three-dimensional spectral signal-to-noise ratio for a class of reconstruction algorithms. *J. Struct. Biol.* **138**, 34–46.

Penczek, P.A., Frank, J. & Spahn, C.M. (2006a) A method of focused classification, based on the bootstrap 3D variance analysis, and its application to EF-G-dependent translocation. *J. Struct. Biol.* **154**, 184–194.

Penczek, P.A., Grassucci, R.A. & Frank, J. (1994) The ribosome at improved resolution: new techniques for merging and orientation refinement in 3D cryo-electron microscopy of biological particles. *Ultramicroscopy* **53**, 251–270.

Penczek, P.A., Renka, R. & Schomberg, H. (2004) Gridding-based direct Fourier inversion of the three-dimensional ray transform. *J. Opt. Soc. Am. A. Opt. Image Sci. Vis.* **21**, 499–509.

Penczek, P.A., Yang, C., Frank, J. & Spahn, C.M. (2006b) Estimation of variance in single-particle reconstruction using the bootstrap technique. *J. Struct. Biol.* **154**, 168–183.

Penczek, P.A., Zhu, J. & Frank, J. (1996) A common-lines based method for determining orientations for N > 3 particle projections simultaneously. *Ultramicroscopy* **63**, 205–218.

Penczek, P.A., Zhu, J., Schroeder, R. & Frank, J. (1997) Three dimensional reconstruction with contrast transfer compensation from defocus series. *Scanning Microsc.* **11**, 147–154.

Philippsen, A., Engel, H.A. & Engel, A. (2007) The contrast-imaging function for tilted specimens. *Ultramicroscopy* **107**, 202–212.

Potter, C.S., Pulokas, J., Smith, P., Suloway, C. & Carragher, B. (2004) Robotic grid loading system for a transmission electron microscope. *J. Struct. Biol.* **146**, 431–440.

Radermacher, M. (1988) Three-dimensional reconstruction of single particles from random and nonrandom tilt series. *J. Electron Microsc. Tech.* **9**, 359–394.

Radermacher, M. (1992) Weighted back-projection methods. *Electron Tomography: Three-Dimensional Imaging with Transmission Electron Microscope* (ed. by J. Frank), pp. 91–115. Plenum Press, New York.

Radermacher, M. (1994) Three-dimensional reconstruction from random projections: orientational alignment via Radon transforms. *Ultramicroscopy* **53**, 121–136.

Radermacher, M., Wagenknecht, T., Verschoor, A. & Frank, J. (1986) A new 3-D reconstruction scheme applied to the 50S ribosomal subunit of *E. coli*. *J. Microsc.* **141**(Pt 1), RP1–2.

Radermacher, M., Wagenknecht, T., Verschoor, A. & Frank, J. (1987) Three-dimensional reconstruction from a single-exposure, random conical tilt series applied to the 50S ribosomal subunit of *Escherichia coli*. *J. Microsc.* **146**(Pt 2), 113–136.

Rath, B.K., Marko, M., Radermacher, M. & Frank, J. (1997) Low-dose automated electron tomography: a recent implementation. *J. Struct. Biol.* **120**, 210–218.

Richter, K. (1994) Cutting artefacts on ultrathin cryosections of biological bulk specimens. *Micron* **25**, 297–308.

Rosenthal, P.B. & Henderson, R. (2003) Optimal determination of particle orientation, absolute hand, and contrast loss in single-particle electron cryomicroscopy. *J. Mol. Biol.* **333**, 721–745.

Ruiz, T. & Radermacher, M. (2006) Three-dimensional analysis of single particles by electron microscopy: sample preparation and data acquisition. *Methods Mol. Biol.* **319**, 403–425.

Saban, S.D., Silvestry, M., Nemerow, G.R. & Stewart, P.L. (2006) Visualization of alpha-helices in a 6-angstrom resolution cryoelectron microscopy structure of adenovirus allows refinement of capsid protein assignments. *J. Virol.* **80**, 12049–12059.

Saibil, H.R. & Ranson, N.A. (2002) The chaperonin folding machine. *Trends Biochem. Sci.* **27**, 627–632.

Sali, A., Glaeser, R., Earnest, T. & Baumeister, W. (2003) From words to literature in structural proteomics. *Nature* **422**, 216–225.

Sartori Blanc, N., Studer, D., Ruhl, K. & Dubochet, J. (1998) Electron beam-induced changes in vitreous sections of biological samples. *J. Microsc.* **192**, 194–201.

Saxton, W.O. & Baumeister, W. (1982) The correlation averaging of a regularly arranged bacterial cell envelope protein. *J. Microsc.* **127**, 127–138.

Scheres, S.H., Gao, H., Valle, M., Herman, G.T., Eggermont, P.P., Frank, J. & Carazo, J.M. (2007) Disentangling conformational states of macromolecules in 3D-EM through likelihood optimization. *Nat. Methods* **4**, 27–29.

Schmidt-Krey, I. (2007) Electron crystallography of membrane proteins: two-dimensional crystallization and screening by electron microscopy. *Methods* **41**, 417–426.

Segui-Simarro, J.M., Austin, J.R., 2nd, White, E.A. & Staehelin, L.A. (2004) Electron tomographic analysis of somatic cell plate formation in meristematic cells of arabidopsis preserved by high-pressure freezing. *Plant. Cell.* **16**, 836–856.

Sorzano, C.O., Jonic, S., Cottevieille, M., Larquet, E., Boisset, N. & Marco, S. (2007a) 3D electron microscopy of biological nanomachines: principles and applications. *Eur. Biophys. J.* **36**, 995–1013.

Sorzano, C.O., Jonic, S., Nunez-Ramirez, R., Boisset, N. & Carazo, J.M. (2007b) Fast, robust, and accurate determination of transmission electron microscopy contrast transfer function. *J. Struct. Biol.* **160**, 249–262.

Sorzano, C.O., Marabini, R., Boisset, N., Rietzel, E., Schroeder, R., Herman, G.T. & Carazo, J.M. (2001) The effect of overabundant projection directions on 3D reconstruction algorithms. *J. Struct. Biol.* **133**, 108–118.

Sorzano, C.O., Marabini, R., Velazquez-Muriel, J., Bilbao-Castro, J.R., Scheres, S.H., Carazo, J.M. & Pascual-Montano, A. (2004a) XMIPP: a new generation of an open-source image processing package for electron microscopy. *J. Struct. Biol.* **148**, 194–204.

Sorzano, C.O.S., Jonic, S., El-Bez, C., Carazo, J.M., De Carlo, S., Thevenaz, P. & Unser, M. (2004b) A multiresolution approach to orientation assignment in 3D electron microscopy of single particles. *J. Struct. Biol.* **146**, 381–392.

Sorzano, C.O.S., Marabini, R., Herman, G.T., Censor, Y. & Carazo, J.M. (2004c) Transfer function restoration in 3D electron microscopy via iterative data refinement. *Phys. Med. Biol.* **49**, 509–522.

Sousa, D. & Grigorieff, N. (2007) Ab initio resolution measurement for single particle structures. *J. Struct. Biol.* **157**, 201–210.

Stagg, S.M., Lander, G.C., Pulokas, J., *et al.* (2006) Automated cryoEM data acquisition and analysis of 284742 particles of GroEL. *J. Struct. Biol.* **155**, 470–481.

Stoffler, D., Feja, B., Fahrenkrog, B., Walz, J., Typke, D. & Aebi, U. (2003) Cryo-electron tomography provides novel insights into nuclear pore

architecture: implications for nucleocytoplasmic transport. *J. Mol. Biol.* **328**, 119–130.

Stoschek, A. & Hegerl, R. (1997) Denoising of electron tomographic reconstructions using multiscale transformations. *J. Struct. Biol.* **120**, 257–265.

Studer, D., Michel, M. & Muller, M. (1989) High pressure freezing comes of age. *Scanning Microsc. Suppl.* **3**, 253–268; discussion 268–269.

Subramaniam, S. & Milne, J.L.S. (2004) Three-dimensional electron microscopy at molecular resolution. *Annu. Rev. Biophys. Biomol. Struct.* **33**, 141–155.

Suloway, C., Pulokas, J., Fellmann, D., *et al.* (2005) Automated molecular microscopy: the new Leginon system. *J. Struct. Biol.* **151**, 41–60.

Tama, F. & Brooks, C.L. (2006) Symmetry, form, and shape: guiding principles for robustness in macromolecular machines. *Annu. Rev. Biophys. Biomol. Struct.* **35**, 115–133.

Tama, F., Miyashita, O. & Brooks, C.L., 3rd. (2004) Normal mode based flexible fitting of high-resolution structure into low-resolution experimental data from cryo-EM. *J. Struct. Biol.* **147**, 315–326.

Tang, G., Peng, L., Baldwin, P.R., Mann, D.S., Jiang, W., Rees, I. & Ludtke, S.J. (2007) EMAN2: an extensible image processing suite for electron microscopy. *J. Struct. Biol.* **157**, 38–46.

Tao, Y. & Zhang, W. (2000) Recent developments in cryo-electron microscopy reconstruction of single particles. *Curr. Opin. Struct. Biol.* **10**, 616–622.

Thuman-Commike, P.A. & Chiu, W. (2000) Reconstruction principles of icosahedral virus structure determination using electron cryomicroscopy. *Micron* **31**, 687–711.

Typke, D., Hegerl, R. & Kleinz, J. (1992) Image restoration for biological objects using external TEM control and electronic image recording. *Ultramicroscopy* **46**, 157–173.

Unser, M., Sorzano, C.O., Thevenaz, P., *et al.* (2005) Spectral signal-to-noise ratio and resolution assessment of 3D reconstructions. *J. Struct. Biol.* **149**, 243–255.

van Heel, M. (1987) Angular reconstitution: a posteriori assignment of projection directions for 3D reconstruction. *Ultramicroscopy* **21**, 111–123.

van Heel, M. & Frank, J. (1981) Use of multivariate statistics in analysing the images of biological macromolecules. *Ultramicroscopy* **6**, 187–194.

van Heel, M., Gowen, B., Matadeen, R., *et al.* (2000) Single-particle electron cryo-microscopy: towards atomic resolution. *Q. Rev. Biophys.* **33**, 307–369.

van Heel, M., Harauz, G., Orlova, E.V., Schmidt, R. & Schatz, M. (1996) A new generation of the IMAGIC image processing system. *J. Struct. Biol.* **116**, 17–24.

van Heel, M. & Schatz, M. (2005) Fourier shell correlation threshold criteria. *J. Struct. Biol.* **151**, 250–262.

van Heel, M. & Stoffler-Meilicke, M. (1985) Characteristic views of *E. coli* and *B. stearothermophilus* 30S ribosomal subunits in the electron microscope. *EMBO J.* **4**, 2389–2395.

Velazquez-Muriel, J.A. & Carazo, J.M. (2007) Flexible fitting in 3D-EM with incomplete data on superfamily variability. *J. Struct. Biol.* **158**, 165–181.

Velazquez-Muriel, J.A., Sorzano, C.O., Fernandez, J.J. & Carazo, J.M. (2003) A method for estimating the CTF in electron microscopy based on ARMA models and parameter adjustment. *Ultramicroscopy* **96**, 17–35.

Walz, J., Typke, D., Nitsch, M., Koster, A.J., Hegerl, R. & Baumeister, W. (1997) Electron tomography of single ice-embedded macromolecules: three-dimensional alignment and classification. *J. Struct. Biol.* **120**, 387–395.

Walz, T. & Grigorieff, N. (1998) Electron crystallography of two-dimensional crystals of membrane proteins. *J. Struct. Biol.* **121**, 142–161.

Wang, H.W. & Nogales, E. (2005) An iterative Fourier-Bessel algorithm for reconstruction of helical structures with severe Bessel overlap. *J. Struct. Biol.* **149**, 65–78.

Wang, L. & Sigworth, F.J. (2006) Cryo-EM and single particles. *Physiology (Bethesda)* **21**, 13–18.

Winkler, H. & Taylor, K. (2006) Accurate marker-free alignment with simultaneous geometry determination and reconstruction of tilt series in electron tomography. *Ultramicroscopy* **106**, 240–254.

Zalokar, M. (1966) A simple freeze-substitution method for electron microscopy. *J. Ultrastruct. Res.* **15**, 469–479.

Zernike, F. (1942) Phase contrast, a new method for the microscopic observation of transparent objects. *Physica* **9**, 686–693.

Zheng, Q.S., Braunfeld, M.B., Sedat, J.W. & Agard, D.A. (2004) An improved strategy for automated electron microscopic tomography. *J. Struct. Biol.* **147**, 91–101.

Zheng, S.Q., Keszthelyi, B., Branlund, E., Lyle, J.M., Braunfeld, M.B., Sedat, J.W. & Agard, D.A. (2007) UCSF tomography: an integrated software suite for real-time electron microscopic tomographic data collection, alignment, and reconstruction. *J. Struct. Biol.* **157**, 138–147.

Zhou, Z.H., Dougherty, M., Jakana, J., He, J., Rixon, F.J. & Chiu, W. (2000) Seeing the herpesvirus capsid at 8.5 Å. *Science* **288**, 877–880.

Zhou, Z.H., Hardt, S., Wang, B., Sherman, M.B., Jakana, J. & Chiu, W. (1996) CTF determination of images of ice-embedded single particles using a graphics interface. *J. Struct. Biol.* **116**, 216–222.

Zhu, Y., Carragher, B., Glaeser, R.M., *et al.* (2004) Automatic particle selection: results of a comparative study. *J. Struct. Biol.* **145**, 3–14.

Zhu, Y., Carragher, B., Kriegman, D.J., Milligan, R.A. & Potter, C.S. (2001) Automated identification of filaments in cryoelectron microscopy images. *J. Struct. Biol.* **135**, 302–312.

Ziese, U., Geerts, W.J., Van Der Krift, T.P., Verkleij, A.J. & Koster, A.J. (2003) Correction of autofocusing errors due to specimen tilt for automated electron tomography. *J. Microsc.* **211**, 179–185.

 